

Forecasting lightning threat using  
cloud-resolving model simulations

by

Eugene W. McCaul Jr. \*  
Universities Space Research Association,  
Huntsville, Alabama

Steven J. Goodman  
NOAA/NESDIS/ORA,  
Camp Springs, Maryland

Katherine M. LaCasse  
University of Alabama in Huntsville,  
Huntsville, Alabama

Daniel J. Cecil  
University of Alabama in Huntsville,  
Huntsville, Alabama

submitted April 2008

revised September 2008

---

\* Corresponding author address: Eugene W. McCaul Jr., Universities Space Research Association, 6767 Old Madison Pike, Bldg. 4, Suite 450, Huntsville, AL 35806. Email: emccaul@usra.edu

## ABSTRACT

Two new approaches are proposed and developed for making time and space-dependent, quantitative short-term forecasts of lightning threat, and a blend of these approaches is devised that capitalizes on the strengths of each. The new methods are distinctive in that they are based entirely on the ice-phase hydrometeor fields generated by regional cloud-resolving numerical simulations, such as those produced by the WRF model. These methods are justified by established observational evidence linking aspects of the precipitating ice hydrometeor fields to total flash rates. The methods are straightforward and easy to implement, and offer an effective near-term alternative to the incorporation of complex and costly cloud electrification schemes into numerical models.

One method is based on upward fluxes of precipitating ice hydrometeors in the mixed phase region at the  $-15^{\circ}\text{C}$  level, while the second method is based on the vertically integrated amounts of ice hydrometeors in each model grid column. Each method can be calibrated by comparing domainwide statistics of the peak values of simulated flash rate proxy fields against domainwide peak total lightning flash rate density data from observations. Tests show that the first method is able to capture much of the temporal variability of the lightning threat, while the second method does a better job of depicting the areal coverage of the threat. Our blended solution is designed to retain most of the temporal sensitivity of the first method, while adding the improved spatial coverage of the second.

Simulations of selected diverse North Alabama cases show that WRF can distinguish the general character of most convective events, and that our methods show promise as a means of generating quantitatively realistic fields of lightning threat. However, because the models tend to have more difficulty in predicting the instantaneous placement of storms, forecasts of the detailed location of the lightning threat based on single simulations can

be in error. Although these model shortcomings presently limit the precision of lightning threat forecasts from individual runs of current generation models, the techniques proposed herein should continue to be applicable as newer and more accurate physically-based model versions, physical parameterizations, initialization techniques and ensembles of forecasts become available.

## 1. Introduction

The threat from lightning in convective storms is a significant source of concern for public safety and a wide range of weather sensitive operations. In the United States alone, lightning is responsible for nearly 1000 deaths and injuries each year, with damages exceeding \$1 billion (Curran *et al.* 2000). As a consequence, improved short-term (0-12h) forecasts of lightning threat are of interest to the National Weather Service (NWS) and other forecasting organizations (Darden *et al.* 2006). Although cloud-to-ground (CG) lightning is of obvious importance to ground-based operations, the total lightning activity (intracloud and CG) has been shown to be useful as an indicator of impending severe or high-impact weather (Goodman *et al.* 2000; Williams *et al.* 1999; Gatlin 2007). With the planned launch in 2014 of a Geostationary Lightning Mapper (GLM) aboard the GOES-R series of Geostationary Operational Environmental Satellites, the exploitation of new applications derived from total lightning measurements will continue to gain interest.

Previous efforts to forecast lightning threat have been based largely on the climatological connections between thunderstorm occurrence and certain parameters of the pre-storm environment. Bright *et al.* (2004), for example, utilized midlevel layer estimates of convective available potential energy (CAPE) to infer likely convective storm upward velocities aloft in their construction of lightning probability maps. However, their approach was used only for finding regions favorable for thunderstorm formation, and could not be used to make quantitative estimates of lightning flash rate within storms. Regression-based methods proposed by Mazany *et al.* (2002) and Burrows *et al.* (2005) are similarly limited. While Bothwell (2005) and Shafer and Fuelberg (2007) also use statistical methods to relate lightning occurrence to aspects of the observed storm environment, they further attempt to classify the amounts of lightning in subjectively defined categories. All these

previous research efforts have focused on the threat from cloud-to-ground lightning.

In recent years, global-scale observing systems such as the Tropical Rainfall Measuring Mission (TRMM) satellite, with its Lightning Imaging Sensor (LIS) and Precipitation Radar (PR), have allowed investigators to document robust relationships between lightning flash rates and the hydrometeor microphysical properties of storms. Cecil *et al.* (2005) showed that the flash rates of storms were closely tied to the amount of radar reflectivity aloft in the ice-phase regions of the storms. Meanwhile, Petersen *et al.* (2005) found a strong relationship between the vertically integrated large precipitating ice content in storms and their lightning flash rates. Fluxes of ice species such as graupel in the mixed phase region near  $-15^{\circ}\text{C}$  have also been shown to be related to storm flash rates (Petersen *et al.* 2005; Deierling and Petersen, 2008). These regime-independent globally-based results are consistent with the more limited regional observations reported by Shackford (1960), Goodman *et al.* (1988; 2005), and others.

Most cloud-resolving numerical models now have the capability of computing fields of mixing ratios of multiple species of hydrometeors, including several important ice-phase species. Thus, cloud-resolving models, such as the Weather Research and Forecasting (WRF; Skamarock *et al.* 2005) model, can now provide time- and space-dependent simulated fields of parameters known to be associated with lightning flash rate. Indeed, cloud-resolving forecast simulations with these capabilities are now becoming commonplace. However, in recognition of the rapid growth of errors in models at convective scales, some recent simulation investigations have even begun to explore the use of cloud-resolving model ensembles (see, e.g., Kong *et al.* 2006).

In this paper, we develop methodologies to demonstrate how regional cloud-resolving forecast simulations can be exploited to create quantitatively calibrated, time-dependent

and specific short-term forecast maps of evolving lightning flash rate density fields in convective environments. Given high-resolution output from a suitable numerical model, our prototype methods yield lightning forecast products that are straightforward, while avoiding the added expense and complexity of incorporating explicit cloud electrification algorithms into the models (see, e.g., Helsdon *et al.* 1987, Helsdon *et al.* 1992, MacGorman *et al.* 2001, Mansell *et al.* 2002, Kuhlman *et al.* 2006). For this prototype research, we restrict our efforts to analysis of a selection of deterministic simulations only. The application of our methods to convective model ensembles is considered beyond the scope of this work, and is relegated to future research.

Two distinct approaches to forecasting the lightning flash rate density field are devised and discussed herein, along with a blended version that attempts to capitalize on the strengths of each. One uses the prognosed field of upward vertical velocity multiplied by graupel mixing ratio at the  $-15^{\circ}\text{C}$  level, hereinafter called “graupel flux,” even though mass units are absent because air density is not used in its evaluation. The second approach exploits the relationship between storm total flash rate and total volumetric amount of precipitating ice. For use on a model grid, we may express this latter relationship in terms of the vertically integrated ice content in each grid column. Other approaches based on regression analysis of satellite-based lightning flash rates against radar reflectivity profiles in storms (see Cecil *et al.* 2005), are also under consideration, but require further analyses of the TRMM PR-LIS databases and additional simulation cases for algorithm development. Both of the techniques reported herein can be empirically calibrated for any given cloud-resolving model configuration, using successful simulations of a few diverse cases for which ground-truth total lightning flash rate densities are known. Because our blended approach is simply a weighted average of methods 1 and 2, it maintains the correct

calibration for peak flash rate densities, while retaining significant temporal sensitivity and ensuring improved capabilities in matching threat areal coverage to the observations.

Results of WRF simulations of various types of Alabama storm systems demonstrate the model's ability to discriminate between convective events of differing depth and intensity, although with the 2 km grid mesh employed here, the model often produces storms that are somewhat weaker and exhibit more areal coverage than those observed. The model's weak bias is compensated for by our flash rate calibration methods, while the model's tendency to produce too much areal coverage of convection does not appear to extend to the deeper convection that is associated with lightning. However, the model also tends to mislocate storms spatially and temporally, and it is not easy to compensate for such phase errors. Because of the limitations of the WRF configuration used here, and of the small sample of cases studied, our calibrations and results here should be regarded as exploratory. Nevertheless, the flash rate prognostic techniques described here show much promise, and can readily be applied to improved future versions of cloud models.

Section 2 explains the data and analysis techniques employed in this study, and presents the basis for our calibrated lightning threat methods. Section 3 applies calibration techniques to our full sample of simulations, thereby obtaining detailed formulae for lightning threat computations, and applies these formulae to two contrasting WRF model case studies. In section 4, we present our blended solution for WRF-based lightning threat, and show how it works for our two selected case studies. In section 5, we give a discussion of our results, and in section 6, we summarize our findings and discuss future research needs.

## 2. Methodology

## a. Numerical simulations

Our numerical simulations are conducted using the WRF model, version 2.1.2, on a native 2-km horizontal mesh having 51 vertical sigma levels. For this model mesh, convection is simulated explicitly; no cumulus parameterization is needed. Other model physical parameterization choices are detailed in Table 1. Of particular importance is the use of the WRF Single-Moment Six Species (WSM-6) microphysics package. In this simplified scheme, water substance can assume only the six forms of vapor, cloud water, rain, cloud ice, snow and either graupel or hail. In our model runs, we have opted to use graupel, with a density of  $300 \text{ kg m}^{-3}$ .

All model runs are initialized using AWIP212 National Centers for Environmental Prediction (NCEP) Eta Data Assimilation System (EDAS) analyses, supplemented with surface and aircraft observations, and also data from the national network of WSR-88D Doppler weather radars. The radial velocity fields from the WSR-88Ds were always used, and reflectivity fields were also tested in some cases where precipitating convection was already occurring at the model start time. Three-hourly forecast fields from NCEP's Eta model were used to obtain updates of model lateral boundary conditions.

WRF integrations were conducted for periods lasting from 6 to 12 h, with 25 time periods saved for analysis. The save interval was 15 min for the 6-h forecast runs. For the 12-h runs, only the last 6-h of the forecast output was saved. This was done because, for the 12-h runs, most of the significant convection occurred more than 6-h into the simulation. One simulation, for the 10 December 2004 cold season hailstorm case discussed herein, was run for 8 h, with output saved at 20 min intervals. Model data were saved as binary files interpolated to a latitude-longitude grid centered near Huntsville, Alabama, and were analyzed using the Grid Analysis and Display (GrADS) software. The mesh spacing for



the interpolated grid was approximately 0.009 degrees in both directions, which equates to 1 km spacing along meridians, approximately twice as fine as the native mesh used in the WRF simulations. The “grid boxes” used in our analyses are therefore slightly smaller than 1 km<sup>2</sup>. The grid mesh contained 447 elements in the zonal direction, and 335 in the meridional direction. Model data were also interpolated in the vertical to yield fields with 500 m vertical mesh spacing, with the lowest level located at 250 m above sea level. On our native 2 km grid, the high terrain of the Appalachian Mountains intrudes several vertical levels into our simulation domain. As a result, all atmospheric data from points located beneath the earth’s surface were treated as missing, and were excluded from our calculations of atmospheric quantities.

Several diverse case studies were selected from the North Alabama region, based on the availability of both model initialization and boundary data and also of “ground-truth” lightning data from the North Alabama Lightning Mapping Array (LMA; Goodman et al. 2005), described briefly below. Results from the simulations showed varying degrees of success. Simulations that we consider as successful featured deep convection of the proper general intensity, with subjectively identified main reflectivity features that appeared to resemble those of the observed storms, and which occurred in the right general area (spatial positioning errors  $O(100 \text{ km})$ ), at the right time (temporal errors  $O(2 \text{ h})$ ). In two other cases, the WRF model failed either to initiate or sustain convection of the proper intensity, and thus did not provide data that could be used to characterize or calibrate the lightning threat associated with the convection. For such cases, it was found that even model runs initialized with radar reflectivity fields failed to generate sustained intense convection. Insofar as the purpose of this research is to demonstrate methods of using cloud-resolving model output as a means of obtaining quantitatively calibrated lightning forecasts - and

not to pursue a validation study of any specific model - we consider here only the successful WRF simulations. For the purposes of documenting our flash rate density forecast calibration methods, we will present results using data from all seven of our successful simulations. For the purposes of showing graphically the character of individual forecasts, however, we will focus on results from two strongly contrasting cases, one featuring a tornadic supercell ahead of a frontal squall line on 30 March 2002, and another featuring smaller and weaker cold-season hailstorms on 10 December 2004. The 30 March 2002 event represents a high flash-rate case, while the 10 December 2004 case represents the low flash-rate end of the spectrum.

#### b. **Lightning observations**

Our ground-truth lightning dataset consists of flash analyses derived from data collected by the North Alabama Lightning Mapping Array (LMA; see e.g., Krehbiel *et al.* 2000). Located in the greater Huntsville, Alabama area, this array consists of 10 sensors that detect VHF pulses from lightning channel segments. After the sensors record the times of received pulses, supplied software (Version 6.2) cross-correlates them and identifies which ones likely correspond to individual physical radiation events. Using this information, the actual time and three-dimensional location of the physical source events comprising lightning flash segments can be estimated (Hamlin, 2004). A flash clustering algorithm is then applied to these chronologically-ordered source data to segregate the large numbers of individual radiation sources into discrete lightning flashes.

The flash algorithm employs time and space proximity criteria to identify which sources are likely to be part of any given flash. Sources are assumed to be part of the same flash if they occur less than 0.3 s apart in time, and also satisfy a spatial separation restriction. This spatial separation criterion is spatially inhomogeneous, to reflect the

differing range and azimuth dependences of the LMA location error, and the range dependence of its detection efficiency characteristics. In addition, consideration is also given to the maximum likely physical spacings between radiating segments of lightning channels, but these spacings are treated as spatially homogeneous, at least in the horizontal. Previous research (Boccippio *et al.* 2000; Thomas *et al.* 2004; Koshak *et al.* 2004), has shown that the source range and altitude uncertainty increase quadratically with range, while the azimuthal error is approximately independent of range. As with the range location uncertainty, the LMA detection efficiency decreases rapidly with range. The physical spacing between radiating segments of lightning channels, meanwhile, can exceed 1 km.

Thus, consideration of the above factors, along with study of the radial stretching of LMA-derived storm footprints with range, suggests that it is appropriate to assume that the maximum allowable total range location difference between successive radiation sources that belong to the same flash increases with the square of range from the network center, such that the range difference is 10 km at a range of 100 km, and 40 km at a range of 200 km. Maximum azimuthal location uncertainties appear to be bounded by 0.05 rad, which is equivalent to 5 km at a range of 100 km. Thus, pairs of sources that satisfy our time difference criterion and also are spaced at ranges that differ by less than our empirical range uncertainty and also at azimuths that differ by less than our empirical azimuthal uncertainty are considered to be part of the same lightning flash. Note that our empirically-derived source-linkage spatial criteria for points in flashes are considerably larger than the simple root-mean-square range and azimuthal errors of individual LMA points documented in Thomas *et al.* (2004). This is due to the need to correctly group most, if not all, the sources belonging to individual flashes, which requires the use of proximity criteria that are much larger than the root-mean-square point location errors of

individual sources. The proximity criteria are also made larger by the range dependence of detection efficiency falloff, and to the inherent variability of the radiative structure of lightning channels. Although our proximity criteria appear generous, tests confirm that they are approximately the smallest that can be chosen without causing spurious increases in flash counts. Furthermore, comparisons with an interactive algorithm developed by New Mexico Tech (see Thomas *et al.* 2003) show that our algorithm's flash counts are within about 5% of theirs, with our algorithm being slightly more conservative.

Because of the rapid increase in range location uncertainty with range from the network center, the ability to map fine-scale spatial structure of flashes diminishes with increasing range from Huntsville. This, however, is not an issue with the present research, where only peak flash count densities are used, and the storms producing these peak values were within 200 km range of the network center. Because of the nature of our flash clustering algorithm, we believe any errors in our flash counts would be manifest as only negligibly small undercounts. These small undercounts are at least partly offset by the possible splitting of some flashes that straddle the beginning times of our 5-min lightning analysis periods.

One issue that complicates interpretation of the derived flash rates is the occurrence of what appear to be single-source flashes. These "singleton" events may be due to errors in correlating weak raw signals identified as being parts of an individual meteorological source, or to errors involving mixing of nonmeteorological pulse detections with meteorological ones (Thomas *et al.* 2004). However, because many singletons are observed to cluster near meteorological targets such as storms, they may also correspond to weak electrical discharges that are not directly associated with stronger, more easily recognized flash events. Because their validity as true independent lightning events is still open to question,

and because they stand out from what appears to be a true background continuum in the spectrum of source numbers per flash, we exclude all singletons from the analyses used in this paper. Thus, we consider valid flashes to have at least two sources.

Once the valid meteorological flashes have been identified, we create gridded time-dependent 2-D horizontal maps of vertically-integrated flash origin density and flash extent density at 5 min intervals on a mesh that matches that of our WRF analyses. Flash origin density, which assigns unit value to the grid cell where a flash initiates, accurately tallies the actual flash rate in a storm, and is used here as a basis for calibration of WRF model proxies against forecast flash rates. Flash extent density, which assigns unit value to each grid cell a given flash traverses (Murphy and Demetriades 2005; Lojou and Cummins 2005), is better suited for gauging the spatial extent of the lightning threat, and is presented here as a means of comparing the areal coverage of observed and forecast lightning threat. It is also a field that is much less sparse than flash origin density, and thus more amenable to graphical display. For these reasons, it is used extensively in our figures describing our actual lightning observations. In all the LMA-based assessments that follow, we propose that a flash extent density of at least  $1.0 \text{ flash traversal } (5 \text{ min})^{-1}$  per grid box column represents an objective minimum threshold above which an observed lightning threat may be said to exist.

Only the flash origin and extent density maps produced at those 5-min time intervals that coincide temporally with the WRF output analysis times are used in direct comparisons with WRF data. These 5-min snapshots of lightning data are similar to what have been used by other researchers in their observational studies of lightning in storms, and represent a good compromise between the brevity needed to reveal trends in storm flash rate, and a duration long enough to provide adequate sampling of the lightning flash rate

in storms, especially in low flash-rate situations.

### c. Calibration of WRF lightning proxies

Based on previous published work (e.g., Petersen et al. 2005), we propose that one useful estimate of the total flash rate may be based on the resolved upward flux  $wq_g$  of large precipitating ice (i.e., graupel) in the mixed phase region at  $-15^\circ\text{C}$ . We designate this first type of threat estimate by the symbol  $F_1$ . For this threat we thus assume:

$$F_1 = f((wq_g)_m) \quad (1)$$

where  $w$  is the vertical velocity,  $q_g$  is the graupel mixing ratio, and the subscript  $m$  attached to the flux implies evaluation at the  $-15^\circ\text{C}$  level in the mixed phase region. Based on published findings and our own results described below in section 3, we will show that the functional dependence symbolized by  $f$  in (1) is well described by a simple linear relationship.

Because the WRF model, like many other cloud-resolving models, cannot be expected to simulate individual convective cells in exactly the same locations and times as observed storms, one cannot use simple scatterplots of individual simulated and observed grid point data to assess the nature of the functional dependence  $f$ . Instead, we assume that in successful simulations the model produces convection which, at its most intense, has a character that is a reasonably faithful rendition of the most intense storms observed anywhere in the domain at any time during the simulation period. We thus compare the maximum gridded observed flash rate to the maximum simulated graupel flux within the simulation time frame to assess the functional form of  $f$ . The results of this comparison and calibration effort are discussed in more detail in Section 3a.

The second model proxy field considered is based on the gridded vertical integral of

graupel, snow and cloud ice. Although the cloud ice field makes relatively little contribution to the amplitude of the lightning flash rate threat, it serves to distribute the associated lightning threat over a wider area, and thus may help account for extended anvil lightning events not readily captured by the graupel flux-based methods, which tend to be more confined to active updraft regions. Thus for our second threat  $F_2$  we have:

$$F_2 = h\left(\int \rho(q_g + q_s + q_i)dz\right) \quad (2)$$

where  $\rho$  is local air density, and  $q_g$ ,  $q_s$  and  $q_i$  are the simulated mixing ratios of graupel, snow and ice, respectively, and  $h$  is a functional relationship that will be shown in Section 3a to be a simple linear proportionality.

### 3. Results

Here we present results of our calibration efforts, followed by data from the two lightning threat algorithms applied to two successful WRF simulation cases. One case is from 00-06 UTC 30 March 2002, when an isolated tornadic supercell erupted in north Alabama equatorward of a broken cold frontal squall line moving through Tennessee. The supercell storm produced the highest peak lightning flash rate observed in any storm from this case, roughly 60 flashes  $\text{min}^{-1}$  just before generating an F-1 tornado near Albertville, Alabama. Expressed in terms of flash origin density, the supercell produced a peak value of 12 flashes  $(5 \text{ min})^{-1}$  per grid box column.

The second case is from 12-20 UTC 10 December 2004, when several small storms produced 2.5 cm hail after an intrusion of destabilizing, cold midtropospheric air advected across the Tennessee Valley region following a cold front. The flash rates from the strongest of these hailstorms were less than 5 flashes  $\text{min}^{-1}$ , and flash densities never exceeded 3 flashes  $(5 \text{ min})^{-1}$  per grid box column. These two cases are chosen to span the approximate

range of severe convective storm event types found in the North Alabama region. Full LMA data were also available for both cases, as were the data needed to launch the WRF simulations.

a. **Calibration of threat indices**

Before interpreting results from our two selected case studies, it is necessary to compare findings from our successful simulations in order to establish reasonable calibration curves for the two lightning threat indices described herein. For threat  $F_1$ , which is based on WRF-simulated graupel fluxes at  $-15^\circ\text{C}$ , we searched each simulation and its corresponding LMA-derived lightning flash rate observations, and extracted the maximum WRF graupel flux and LMA flash rate density from each, plotting them as single points in Fig. 1. Objective least-squares fits of the data using reduced major axis regression techniques indicate that, for both  $F_1$  and  $F_2$ , the 95% confidence limits contain the origin. Based on this, we devised linear regressions with intercepts at the origin for both our threats, and both regressions are found to be significant at more than the 99% confidence level. The slope thereby obtained for the  $F_1$  line is found to be 0.042. The raw cross-correlation between LMA flash rate and graupel flux is 0.67, with rather tight clustering of the data near lower values of each variable, but with enhanced scatter at large values.

Based on the findings from Fig. 1, we propose that the functional relationship in (1) can be well described by the simple linear equation:

$$F_1 = k_1(wq_g)_m \tag{3}$$

where the coefficient  $k_1$  is the 0.042 slope of the line plotted on the figure.

Following the calibration of lightning threat amplitude as in (3), we now consider the separate issue of threat areal coverage. To generate a threat field that has both reasonable



areal coverage and peak flash rate threat values, it is necessary to set a nonzero lower limit for the proxy threat field, which is equivalent to establishing a threshold contour for the field when plotted on a map. Values of the field that lie below this threshold are considered to pose no lightning threat, and are not contoured on our field map plots presented below. For both lightning threats, the optimum threshold contour levels are different, and are identified empirically via experimentation. For threat  $F_1$ , we find a threshold value of 0.01 predicted flash origin points  $(5 \text{ min})^{-1}$  per grid box column to be the best that can reasonably be obtained. This threshold often leads to an underprediction of threat area, an issue which is discussed in more detail in section 5. However, it is probably as small a value as should be considered; sensitivity tests show that further reduction provides little or no increase in areal coverage of this threat.

We follow a similar procedure in Fig. 2 for threat  $F_2$ , which is based on gridded vertically integrated ice content from the WRF. Calibration procedures similar to those described above again indicate that the function  $h$  can be satisfactorily modeled as a linear proportionality, similar to what was found for threat  $F_1$  except for the value of the proportionality constant. The data points used in this calibration are shown in Fig. 2. For threat  $F_2$ , we thus have:

$$F_2 = k_2 \int \rho(q_g + q_s + q_i) dz \quad (4)$$

where the integration is over the full storm depth. From Fig. 2, our zero-intercept regression calculations indicate that the constant  $k_2$  may be estimated as 0.20. For Fig. 2, the objective raw cross-correlation between the LMA flash density and the values of vertically integrated ice is 0.83. In evaluating the areal coverage of threat  $F_2$ , we find that a contouring threshold of 0.40 predicted flash origin points  $(5 \text{ min})^{-1}$  per grid box column provides approximately correct areal coverage for this threat. This threshold implies a

need for at least  $2.1 \text{ kg m}^{-2}$  of vertically integrated ice through the depth of storm anvils for the existence of a lightning threat there.

**b. Spring supercell and squall line**

At 0000 UTC on 30 March 2002, a warm, moist and unstable airmass was in place over the Tennessee Valley region, with a cold front approaching from the northwest. A capping inversion prevented storm formation until near sunset, when an isolated supercell erupted near Tupelo, Mississippi, and moved east into Alabama. Shortly afterwards, new severe storms quickly developed near the Smoky Mountains in eastern Tennessee, while other severe storms built along the cold front in middle Tennessee. The supercell passed south of Huntsville, Alabama, and went on to produce an F-1 tornado west of Albertville, Alabama, after 0520 UTC.

The WRF model produces a representative depiction of these developments during the 6-h forecast launched at 0000 UTC 30 March. A plot of the WRF sounding valid at (latitude, longitude) = (34.4, -88.1) and 0300 UTC 30 March 2002 (Fig. 3) indicates that CAPE of more than  $2000 \text{ J kg}^{-1}$ , along with moderate veering shear, was present in northern Alabama to support the severe convection. The reflectivity field (Fig. 4, gray shades) observed by the NWS Doppler radar at Hytop, Alabama, (KHTX) at 0400 UTC indicates peak low-level reflectivities near or above 60 dBZ in both the supercell at (latitude, longitude) = (34.5, -86.7) and in portions of the other convective lines. LMA-derived flash origin densities reach a peak of  $10 \text{ flashes (5 min)}^{-1}$  per grid box column in the supercell at 0400 UTC, with an absolute peak of 12 having been reached earlier at 0145 UTC. However, as stated earlier, because of the sparseness of the field of flash origin density, we opt to depict the lightning activity in terms of flash extent density (Fig. 4, contours). We also show on Fig. 4 the areal coverage fraction of the LMA-derived flash

extent density field exceeding our minimum plotted contour, which represents 1.0 flash traversal  $(5 \text{ min})^{-1}$  per grid box column. The coverage fraction for this contour threshold turns out to be 0.148, which means that LMA observations indicate that 14.8% of the area of the analysis domain experienced actual lightning threat, either at the ground or overhead, over the 5-min period beginning at 0400 UTC.

In Fig. 5 we present the fields of WRF-derived reflectivity at  $-15^\circ\text{C}$  (grayshades) and predicted flash origin density  $F_1$  (color contours), valid at 0400 UTC 30 March. The areal coverage of the predicted  $F_1$  flash rate field in Fig. 6 is 0.085, which is approximately 60% of the actual observed flash extent density coverage in Fig. 4. It is, however, much larger than the coverage of the observed flash origin density for this event (not shown), which is less than 0.005. On the other hand, the domainwide areal fractions of the predicted and observed lightning threats are much smaller than the areal fraction of positive CAPE, which is 0.64. In section 4, we will discuss the significance of the areal coverage discrepancies between the predicted and observed flash density. We emphasize here that our calibration methods yield predicted flash densities that are strictly referenced to observations of flash origin density, with the threat areal coverage referenced to the areal coverage of observed flash extent density.

Fig. 6 contains a map of contoured lightning threat  $F_2$ , based on the vertical integral of simulated ice, superimposed on the simulated field of anvil-level (near 9 km) cloud ice (shaded). Areal coverage fraction of this threat field, just under 0.158, is also indicated on the plot. It is somewhat larger than that for the first threat field, and is very close to the observed threat coverage shown in Fig. 4.

To check for overall agreement of the intensity forecasts of the lightning threat, we present in Fig. 7 the time series of domain-wide peak values of LMA-derived flash origin

density along with the corresponding predicted peak values from the two threat methods  $F_1$  and  $F_2$ . From Fig. 7 we observe that WRF takes at least 60 min to begin to produce its first predicted lightning, with a large increase in predicted lightning at 90 min, which lags the observations in this regard. Once deep convection is fully established in the WRF model, both threat methods deliver flash rate density values within the range of the LMA observations, although the actual peak of LMA flash rate density occurs rather early on in the simulation period (just before 120 min), when WRF is still developing deep convective cells. There is substantial temporal variability in both the LMA-derived peak flash density and the predicted peak values of  $F_1$ , but much less temporal variability in the predicted peak values of  $F_2$ , which tend to plateau near their maximum values.

Fig. 8 contains the time series plots of LMA-observed flash extent density areal coverage fraction that result when we apply the threshold of 1.0 flash traversals  $(5 \text{ min})^{-1}$  per grid box column, our postulated lower limit in section 2b for observable lightning threat. Also plotted are the areal coverage fractions for threats  $F_1$  and  $F_2$ , each thresholded by the amounts mentioned in section 3a. All the areal coverage time series are more slowly varying than the peak threat value time series of Fig. 7. Of additional interest is the extended time lag seen in the onset of significant areal coverage of lightning threat, as compared to the onset times of the intense but localized lightning threat peaks in Fig. 7. There are also more general temporal mismatches in the times of local peak observed and predicted lightning threat coverage, reinforcing our earlier caveats about the limitations of single individual numerical simulations as forecast tools for real-world convective-scale events. Finally, the peak areal coverage values for threat  $F_1$  are still somewhat too small compared to observed coverage values, suggesting that the threshold contours arrived at for  $F_1$  (see Section 3a) might be too large. However, because this proxy threat field is so

closely tied to strong updraft cores, it was found that lowering its threshold failed to yield useful increases in its corresponding areal coverage.

### c. Cold season hailstorm

On 10 December 2004, a cold airmass aloft moved into the Tennessee Valley, with sufficient lingering warmth and moisture at low levels to allow for the formation of shallow but moderately intense convection. The storms formed just after midmorning (1530 UTC) in Tennessee, with additional storms forming in north Alabama around local noon (1800 UTC). With a cold atmospheric profile aloft (Fig. 9), the storms had approximately  $500 \text{ J kg}^{-1}$  of CAPE with which to build updrafts. Some of the storms produced hail at the surface as large as 2.4 cm in diameter, according to reports in Storm Data. Maximum low-level reflectivities observed by KHTX reached approximately 58 dBZ (see Fig. 10 for representative data from 1900 UTC). The total lightning flash rates from the several storms remained rather small, however, never exceeding  $5 \text{ flashes (min)}^{-1}$  even in the strongest cells. Observed peak flash origin densities never exceeded  $3 \text{ flashes (5 min)}^{-1}$  per grid box column, as suggested by the modest amplitudes of the flash extent density field. Observed flash extent density in excess of  $1.0 \text{ traversals (5 min)}^{-1}$  per grid box displays areal coverage of only 0.018. Both the peak flash densities and areal coverages for this event are more than a factor of 4 smaller than those for the 30 March 2002 case.

In the 8-h simulation launched at 1200 UTC 10 December 2004, the WRF model does well at capturing the location, intensity and character of the deep convection, but shows some error in the timing of its initiation. In the WRF results, for example, deep convection begins after  $t = 200 \text{ min}$  (around 1520 UTC) in Tennessee. In the observations, however, a few brief, weak storms are seen there as early as  $t = 60 \text{ min}$  (1300 UTC), becoming more widespread only after  $t = 320 \text{ min}$  (1720 UTC). By  $t = 360 \text{ min}$  (1800 UTC), both

the WRF and observations indicate additional deep convection developing in northeastern Alabama. All the storms occur in the form of small isolated cells, with some clustering into short lines. At 1900 UTC, the field of surface-based pseudoadiabatic CAPE from WRF (not shown) reveals a large region of values reaching near  $400 \text{ J kg}^{-1}$ , with a predicted lightning threat field  $F_1$  concentrated into small patches associated with just a few of the cells (Fig. 11). As with the 30 March 2002 case, areal coverage of the predicted lightning flash density  $F_1$  (0.012) falls somewhat short of the observed coverage of flash extent density (0.018). In addition, the predicted and observed lightning threat areas are again much smaller than the area of positive CAPE (domain fractional coverage of 0.60) simulated by WRF.

Fig. 12 shows the anvil-level cloud ice field near  $z = 5 \text{ km}$ , along with the computed lightning threat field  $F_2$ , based on column-integrated ice. As in Fig. 6, areal coverage of the threat is expanded relative to the other two threat fields, reaching a fractional coverage of 0.016. Even though there is considerable ice aloft in the western half of the domain, threat  $F_2$  correctly predicts that all the lightning is confined to the northeastern and eastern portions of the WRF simulation region.

The 8-h time series of domainwide maximum observed flash origin density for the 10 December 2004 event is presented in Fig. 13, along with the time series of maximum predicted flash origin density from methods  $F_1$  (THREAT1) and  $F_2$  (THREAT2). The time series plots reiterate that WRF is approximately 2 h too fast in developing multiple deep convective storms in the domain, although a few isolated weak observed storms are found even before the onset of the multiple simulated storms. The peak flash rate densities of threat  $F_1$  are only about half those of the observations, while threat  $F_2$  yields peak flash rate densities much closer to those observed. None of the predicted peak flash rates

from Figs. 7 and 13, however, matches the observed peaks exactly, because of the fact that neither of the two cases presented here have predicted peak values that fall directly on the consensus calibration curves of Figs. 1-2.

Fig. 14 portrays the 8-h time series of the areal coverage fractions of observed and predicted lightning threat for this case. Note that the vertical axis of Fig. 14 has a much smaller range than Fig. 8, because of the much smaller and more localized lightning threat coverage in the 10 December 2004 event. The figure shows clearly that the weak, early storms seen in the observations have negligible areal coverage in the domain, and that the WRF model develops more widespread storminess approximately 2 h earlier than indicated by the observations. The limited areal coverage of lightning threat in this event also poses a challenge to our prognoses of threat coverage, with Threat  $F_2$  exhibiting a fractional peak of 0.023, some 26% smaller than the observed peak of 0.031. As with the much more vigorous 30 March 2002 case, Threat  $F_1$  predicts coverage even smaller than  $F_2$ . As before, however, both our prognostic threat fields exhibit much more restricted and specific coverage than more traditional convection indicators such as positive CAPE, whose coverage fraction at 19 UTC, the time of Figs. 10-12, is 0.60.

#### 4. Blending of calibrated threats

Results from the previous section demonstrate that threat  $F_1$ , which is based on WRF graupel flux at  $-15^\circ\text{C}$ , captures much of the temporal variability of observed peak lightning flash density in the mature convection, but underestimates the areal coverage of the actual lightning activity. Threat  $F_2$ , meanwhile, based on vertically integrated ice, including anvil cirrus, captures the areal coverage of lightning activity well, but portrays the temporal variability of the lightning flash rates less accurately than does  $F_1$ , because it is a vertically integrated quantity. We are thus motivated to construct a blended threat

index that retains the temporal sensitivity of  $F_1$  and better captures the areal coverage of  $F_2$ .

Because both  $F_1$  and  $F_2$  have been calibrated against peak lightning flash rate density, any weighted combination of the two threat fields will also be properly calibrated as well. To retain as much of the temporal variability inherent in threat  $F_1$ , however, any blended threat should probably be weighted heavily toward  $F_1$ . On the other hand, even a lightly weighted contribution by the  $F_2$  field should suffice to provide the desired increase in net areal coverage to the blended threat  $F_3$ , after proper thresholding. We thus propose that a workable blended threat  $F_3$  could be based upon:

$$F_3 = r_1 F_1 + r_2 F_2 \quad (5)$$

where  $r_1 = 0.95$  and  $r_2 = 0.05$ , based on results of sensitivity tests of the effects of various weight choices on resulting peak flash rate densities and areal coverages. Application of (5) to the WRF data for 04 UTC, 30 March 2002, yields the threat field  $F_3$  shown in Fig. 15. Application of a minimum threshold flash rate density of  $0.02 \text{ flash origins } (5 \text{ min})^{-1}$  per grid box column - the first contour plotted in Fig. 15 - yields very good agreement between the predicted (0.17) and observed (0.15) lightning threat coverages. The time series of predicted and observed peak flash densities for  $F_3$  for the 30 March 2002 case are shown in Fig. 16, while the predicted and observed threat areal coverage time series are given in Fig. 17. As expected and desired, the areal coverage for  $F_3$  is larger than for  $F_1$  (see Fig. 5), and approaches that of  $F_2$ , while the accuracy of the  $F_3$  peak flash rate density is unchanged, even as most of the temporal sensitivity of  $F_1$  is retained (see Fig. 17).

The blended threat  $F_3$  works almost as well for the low flash-rate case of 10 December



2004. Fig. 18 shows the field of predicted threat  $F_3$  at 19 UTC, while Figs. 19 and 20 present the time series of observed and predicted peak flash rate densities and threat areal coverages, respectively. The same threshold as in Figs. 15 and 17,  $0.02 \text{ flash origins (5 min)}^{-1}$  per grid box column, was used in assessing threat areal coverage. Although  $F_3$  still underpredicts the peak areal coverage for this case (0.02 versus 0.03 observed), the threat predictions based on  $F_3$  perform better than those from  $F_1$  or  $F_2$  alone, despite the inherent challenges posed by the very low flash rates.

## 5. Discussion

In general, caution is always warranted when dealing with small sample sizes, as is the case in the calibration efforts herein. In both our calibration charts (Figs. 1 and 2), we have modeled the relationship between the two variables as linear, but it is possible that nonlinear behavior might emerge if a larger data sample were available. This is considered a possibility in light of the behavior of the rightmost data point in Fig. 1, which has a graupel flux of  $400 \text{ m s}^{-1}$ , but falls below the regression line. This particular point derives from a simulation for a severe squall line that occurred on 31 May 2004, and is characterized by our largest updraft strengths and largest environmental CAPE values. It is possible that the model's lack of representation of the hail species may have led to an overproduction of graupel for this intense storm system simulation, although additional cases featuring very large CAPE would be needed to confirm this speculation.

Despite the uncertainties attending our small sample of cases, the methods used to devise the lightning threat proxy fields  $F_1$  and  $F_2$  still appear to yield useful approximate indicators of the lightning threat. Our blended threat  $F_3$  appears to mitigate the shortcomings of the threats  $F_1$  and  $F_2$ , by using a judicious weighted average of the two basic threat fields. By design,  $F_3$  tends to match the peak flash rate densities in storm systems,

but it also provides a realistic match for lightning threat areal coverage, while retaining most of the temporal variability of lightning in observed mature storms. It should be noted, however, that our threat  $F_3$  should not be expected to match either the observed peak flash rate densities or threat areal coverages exactly for any specific storm cases, because of the statistical character of our calibration methods. For example, the peak values of  $F_3$  in Figs. 16 and 19 both lie below those of the observed peak flash densities. This is simply because both these observed cases happened to produce peak flash rate densities that fell above the least squares best fit calibration line of Fig. 1. The behavior of the threat areal coverage can differ, however, from that of peak flash rate density, as seen in Figs. 17 and 20, where the predicted peak areal coverages are above and below those observed, respectively. When examining the values in instantaneous snapshots of data, matches can exhibit even more error, owing to the inability of the model to place convective storms of exactly the right intensity in exactly the right place at exactly the right time.

All our threats also exhibit a much more confined areal coverage than other traditional environmental measures used in predicting the likelihood of thunderstorms, such as CAPE. Although the areal coverage of CAPE often overestimates the areal coverage of lightning threat, as in cases where capping or large-scale subsidence are present, it is often considered an important field to examine, because of the possibility that small-scale forcing might overcome the capping and allow for deep convection. For the cases presented here, positive CAPE existed over approximately 60% of the domain at any given time, but the actual instantaneous lightning threat area, as measured by the LMA flash extent density fields and reproduced by threat  $F_3$ , never exceeded 16% coverage. When viewed in a time-integral sense over the course of all seven simulations, CAPE in excess of  $100 \text{ J kg}^{-1}$  covered 88-100% of the domain, but time-integrated lightning threat covered only about 10-30% of the

domain for cases not involving major squall lines, and about 50-80% for squall line cases. These statistics give some idea of how important it is to avoid unnecessary overestimation of the area subject to the forecast lightning threat.

Interestingly, our blended lightning threat coverage tended to be similar to the coverage of the 20 dBZ and greater reflectivity area, and noticeably larger than the area within the 35 dBZ reflectivity isopleth. The latter, for example, was only 11% for the storms in Fig. 5, while the actual observed lightning threat coverage at that time was approximately 15%. The 35 dBZ area thus appears to resemble more closely the area covered by our graupel-flux-based threat  $F_1$  alone (8.5%), although the former is still somewhat larger than the latter. Nevertheless, our observations of lightning threat indicate that ice detrained in storm anvils, which is accounted for by threat  $F_2$  and its contribution to the blended threat  $F_3$ , should not be neglected in the assessment of total lightning threat.

Note that although the blended lightning threat area is close to being coincident with the area of greater than 20 dBZ echo, the use of simple radar reflectivity thresholds to estimate lightning threat is far from straightforward. Our tests of reflectivity as a possible lightning proxy field suggest that nonlinearities are present in the calibration curves; in addition, there are difficulties in finding storm cases where the peak reflectivity did not migrate to high values, frustrating our attempts at constructing evenly populated calibration curves. Likewise, it is difficult to compare our apparent dBZ-based lightning threat spatial extent thresholds with other research dealing with dBZ thresholds for lightning onset (see, e.g., Buechler and Goodman 1990), which commonly infer a need for at least 40 dBZ in the mixed phase region. However, our finding that lightning threat areal coverage approximately matches the area inside the 20 dBZ reflectivity isopleth is not inconsistent with the 40 dBZ lightning onset threshold; an interpretation consistent with our data is

that, while threat areal coverage roughly matches the 20 dBZ or greater area, at least some part of the threat zone must contain 40 dBZ or greater in the mixed phase region. Another way of viewing this situation is that lightning generally requires at least 40 dBZ for initiation, but it can often propagate out into regions of as little as 20 dBZ reflectivity.

Our lightning threat computation methods also exhibit a positive bias in the mean, which is visible in the various time series plots of predicted and observed peak flash density (Figs. 7, 13, 16 and 19). This bias is an inevitable consequence of our choice to design our threats to match the peak flash densities, rather than the averages, in our storm cases. Although our main justification for this design choice is that the most intense storms are of greater concern than others, a secondary justification is that it is problematic to define a meaningful “average” flash density. Our methodology thus tends to overpredict mean flash densities, but this also provides a conservative design, from a warning point of view. Similarly, our threat methods will, when integrated spatially over a storm cell’s instantaneous footprint, tend to produce small overestimates of storm cell flash rate.

The calibration of our prognosed fields of lightning threat is simple, but not without issues requiring careful attention. In particular, the determination of the calibration constants should be performed anew whenever a new model or significantly different version of a previously used model is employed. Previous work (Weisman *et al.* 1997; Bryan *et al.* 2003) has shown how simulated field quantities can vary in amplitude as the model mesh is made coarser or finer. At this point, there is no general method for predicting quantitatively the amount of variation in field amplitudes that is realized when the model mesh changes. All that can be said is that, when comparing to quantities derived from the 2 km native model mesh used here, most field quantities will grow (shrink) in peak amplitude, probably by some tens of percent, as the model mesh is, say, halved (doubled).

We thus emphasize that the specific calibration constants presented herein may not generally provide optimum results for model configurations other than the one discussed in this study. On the other hand, the general approaches that we have outlined here are firmly based on storm physics and should have some general regime-independent validity. As cloud models, initialization procedures, and data assimilation techniques improve, and more lightning cases are archived and analyzed, we expect that the functional relations and diagnosed constants described here will evolve toward greater accuracy and generality, and that overall model capability to predict lightning threat quantitatively will improve.

Although we found that the WRF model did not always produce successful simulations of observed convection, even for some severe convective events, the difficulties in obtaining reliable simulations of less intense convective events were even more challenging. Yet both high flash-rate and low flash-rate cases are needed in order to make robust algorithm calibrations. We continue to explore our data archives for other low-end cases that might yield additional insights.

## 6. Summary and Outlook

We have presented evidence that application of simple physics-based lightning concepts to the calibration of fields output by cloud-resolving models can provide quantitatively calibrated maps of lightning threat for use by forecasters. These simple methods have the potential to allow for useful short-term lightning threat forecasts, without the need for adding expensive and complex electrification subroutines to cloud-resolving models. Drawbacks include the fact that individual simulations tend to do an imperfect job at locating and timing convective storms, and that the cloud-resolving model output that is used to forecast lightning threat may need to be recalibrated against observed lightning data for major changes to the model grid mesh and physics. Intrinsic model errors also

introduce uncertainty into the values of the calibration constants needed in constructing model-based lightning threat forecasts.

Many of the shortcomings of the present WRF model are likely to be alleviated, at least in part, by future improvements to the model physical parameterizations. In particular, a more sophisticated double-moment cloud microphysics scheme that includes at least some form of hail in addition to graupel, would be desirable. Of course, if more species of large precipitating ice are included, our algorithms must be modified to include their effects, even though the graupel species, along with small hail, likely do most of the work in the charge separation process. Running the model on a finer grid mesh would probably also be beneficial in removing the small weak bias seen in the current model storms. Even when these improvements are made, however, some significant errors may well remain, owing to the imperfections in the initial and lateral boundary condition fields used to run the simulations.

In the future, we suggest that some of the uncertainties associated with the model data can be addressed by running small ensembles using diverse choices for microphysics and boundary layer schemes, and, if possible, initial conditions. Probability-based analysis of the patterns of convection found across such ensembles will allow for objective statistical assessment of the skill of our lightning threat methods in prospective future case studies or operational settings. Although studies using results from ensembles of simulations are considered a top priority, experiments with newer versions of the WRF model and other cloud-resolving models are also contemplated. In addition, we seek to identify and analyze other new cases of very low, intermediate, and very high flash-rate storm events, and to run cloud-resolving simulations on them for the purpose of refining our empirical estimates of the functional forms and curve-fitting coefficients of our various lightning

threat predictors. In particular, we are also in the process of reanalyzing the database of Cecil et al. (2005) to obtain lightning-reflectivity relationships based on gridded data, rather than storm system precipitation features, and to construct additional lightning threats based on reflectivity profile shape. Finally, the existence of simple, apparently invertible linear relationships between total flash rate density and parameters such as graupel flux and vertically integrated ice suggest opportunities for ways to convert observed lightning flash rate data from satellite-based sensors such as GLM into forms that can be assimilated into operational forecast models.

## 7. Acknowledgments

This research was funded by NASA Science Mission Directorate's Earth Science Division in support of the Short-term Prediction and Research Transition (SPoRT) Project at Marshall Space Flight Center, Huntsville, AL. We also thank the NOAA GOES-R Program Office for the funding it provided in support of GOES-R Lightning Mapper risk reduction science, under Space Act Agreement Order NA07AANEG0284. The authors have also benefitted from helpful discussions with Paul Krehbiel and Ron Thomas, New Mexico Tech, Walt Petersen and Kevin Doty, UAH, Bill Koshak and Rich Blakeslee, NASA Marshall Space Flight Center, and Morris Weisman, NCAR, during the course of this research. Kelvin Droegemeier and Kevin Thomas, Univ. of Oklahoma, provided sample high-resolution WRF datasets for test purposes early in the work. Jayanthi Srikishen, USRA Huntsville, assisted in installation of the WRF model code. The views, opinions, and findings contained herein are those of the authors, and should not be construed as an official NASA, NOAA or U. S. Government position, policy, or decision.



## REFERENCES

- Boccippio, D. J., W. Koshak, R. Blakeslee, K. Driscoll, D. Mach, D. Buechler, W. Boeck, H. J. Christian, and S. J. Goodman, 2000: The Optical Transient Detector (OTD): Instrument characteristics and cross-sensor validation. *J. Atmos. Oceanic Technol.*, **17**, 441–458.
- Bothwell, P., 2005: Development of an operational statistical scheme to predict the location and intensity of lightning. *Preprints, Conf. on Meteorol. Applications of Lightning Data*, San Diego, CA, Amer. Meteor. Soc.
- Bright, D. R., M. S. Wandishin, R. E. Jewell, and S. J. Weiss, 2004: A physically based parameter for lightning prediction and its calibration in ensemble forecasts. *Preprints CD-ROM*, 22nd Conf. Severe Local Storms, Hyannis, MA, Amer. Meteor. Soc., paper 4.3.
- Bryan, G. H., J. C. Wyngaard and J. M. Fritsch, 2003: Resolution requirements for the simulation of deep moist convection. *Mon. Wea. Rev.*, **131**, 2394–2416.
- Buechler, D. E., and S. J. Goodman, 1990: Echo size and asymmetry: Impact on NEXRAD storm identification. *J. Appl. Meteorol.*, **29**, 962–969.
- Burrows, W. R., C. Price, and L. J. Wilson, 2005: Warm season lightning probability prediction for Canada and the northern United States. *Wea. Forecasting*, **20**, 971–988.
- Cecil, D. J., S. J. Goodman, D. J. Boccippio, E. J. Zipser, and S. W. Nesbitt, 2005: Three years of TRMM precipitation features. Part I: Radar, radiometric, and lightning characteristics. *Mon. Wea. Rev.*, **133**, 543–566.
- Curran, E. B., R. L. Holle, and R. E. Lopez, 2000: Lightning casualties in the United States from 1959 to 1994. *J. Climate*, **13**, 3448–3453.
- Darden, C. B., P. Gatlin, J. Burks, S. Goodman, D. E. Buechler and J. Hall, 2006: Total

lightning in the warning decision making process - Two years of case studies. *Preprints CD-ROM*, 2nd Conf. Meteorol. Appl. Lightning Data, Atlanta, GA, Amer. Meteor. Soc., paper P1.1.

Deierling, W., and W. A. Petersen, 2008: Total lightning activity as an indicator of updraft characteristics. *J. Geophys. Res.*, accepted.

Gatlin, P. N., 2007: Severe weather precursors in the lightning activity of Tennessee Valley thunderstorms. M.S. thesis, Dept. of Atmospheric Science, The University of Alabama in Huntsville, 99 pp. [Available from The UAH Library, 301 Sparkman Dr., Huntsville, AL 35899 or online at [http://vortex.nsstc.uah.edu/public/outgoing/gatlin/thesis/thesis\\_gatlin\\_2007.pdf](http://vortex.nsstc.uah.edu/public/outgoing/gatlin/thesis/thesis_gatlin_2007.pdf)]

Goodman, S. J., D. E. Buechler, P. D. Wright, and W. D. Rust, 1988: Lightning and precipitation history of a microburst-producing storm. *Geophys. Res. Lett.*, **15**, 1185–1188.

Goodman, S. J., D. E. Buechler, K. Knupp, K. Driscoll, and E. W. McCaul, Jr., 2000: The 1997-98 El Nino event and related wintertime lightning variations in the Southeastern United States. *Geophys. Res. Lett.*, **27**(4), 541–544.

Goodman, S. J., R. Blakeslee, H. Christian, W. Koshak, J. Bailey, J. Hall, E. McCaul, D. Buechler, C. Darden, J. Burks, T. Bradshaw, and P. Gatlin, 2005: The North Alabama Lightning Mapping Array: Recent severe storm observations and future prospects. *Atmos. Res.*, **76**, 423–437.

Hamlin, T. D., 2004: The New Mexico Tech Lightning Mapping Array. Ph.D. dissertation, New Mexico Inst. Mining and Technol., 164 pp.

Helsdon, J. H. Jr., and R. D. Farley, 1987: A numerical modeling study of a Montana thunderstorm: 2. Model results versus observations involving electrical aspects. *J. Geophys. Res.*, **92**, 5661–5675.

- Helsdon, J. H. Jr., G. Wu, and R. D. Farley, 1992: An intracloud lightning parameterization scheme for a storm electrification model. *J. Geophys. Res.*, **97**, 5865–5884.
- Kong, F., K. Droegemeier, and N. Hickmon, 2006: Multiresolution ensemble forecasts of an observed tornadic thunderstorm system. Part I: Comparison of coarse- and fine-grid experiments. *Mon. Wea. Rev.*, **134**, 807–833.
- Koshak, W. J., R. J. Solakiewicz, R. J. Blakeslee, S. J. Goodman, H. J. Christian, J. M. Hall, J. C. Bailey, E. P. Krider, M. G. Bateman, D. J. Boccippio, D. M. Mach, E. W. McCaul, M. F. Stewart, D. E. Buechler, W. A. Petersen, and D. J. Cecil, 2004: North Alabama Lightning Mapping Array (LMA): VHF source retrieval algorithm and error analyses. *J. Atmos. Oceanic Technol.*, **21**, 543–558.
- Krehbiel, P.R., R.J. Thomas, W. Rison, T. Hamlin, J. Harlin, and M. Davis, 2000: GPS-based mapping system reveals lightning inside storms. *Eos*, **81**, 21–25.
- Kuhlman, K., C. Ziegler, E. Mansell, D. MacGorman, and J. Straka, 2006: Numerically simulated electrification and lightning of the 29 June 2000 STEPS supercell storm. *Mon. Wea. Rev.*, **134**, 2734–2757.
- Lojou, J.-Y., and K. L. Cummins, 2005: On the representation of two- and three-dimensional total lightning information. *Preprints CD-ROM*, 1st Conf. Meteorol. Appl. Lightning Data, San Diego, CA, Amer. Meteor. Soc., paper 2.4.
- MacGorman, D. R., J. M. Straka, and C. L. Ziegler, 2001: A lightning parameterization for numerical cloud models. *J. Appl. Meteor.*, **40**, 459–478.
- Mansell, E. R., D. R. MacGorman, C. L. Ziegler, and J. M. Straka, 2002: Simulated three-dimensional branched lightning in a numerical thunderstorm model. *J. Geophys. Res.*, **107**, 4075, doi: 10.1029/2000JD000244.
- Mazany, R. A., S. Businger, S. I. Gutman, and W. Roeder, 2002: A lightning prediction index that utilizes GPS integrated precipitable water vapor. *Wea. Forecasting*, **17**,

- Murphy, M. J., and N. Demetriades, 2005: An analysis of lightning holes in a DFW supercell storm using total lightning and radar information. *Preprints CD-ROM*, 1st Conf. Meteorol. Appl. Lightning Data, San Diego, CA, Amer. Meteor. Soc., paper 2.3.
- Petersen, W. A., H. J. Christian, and S. A. Rutledge, 2005: TRMM observations of the global relationship between ice water content and lightning. *Geophys. Res. Lett.*, 26 July 2005, **32**;14, L14819 doi: 10.1029/2005GL023236.
- Shackford, C. R., 1960: Radar indications of a precipitation-lightning relationship in New England thunderstorms. *J. Atmos. Sci.*, **17**, 15–19.
- Shafer, P. E., and H. E. Fuelberg, 2008: A perfect prognosis scheme for forecasting warm season lightning over Florida. Part I: Model development. *Mon. Wea. Rev.*, **136**, 1817–1846.
- Skamarock, W. C., J. B. Klemp, J. Dudhia, D. O. Gill, D. M. Barker, W. Wang, and J. G. Powers, 2005: A description of the Advanced Research WRF Version 2. NCAR Technical Note NCAR/TN-468+STR, 100 pp.
- Thomas, R., P. Krehbiel, W. Rison, J. Harlin, T. Hamlin, and N. Campbell, 2003: The LMA flash algorithm. *Proc., 12th Int. Conf. on Atmos. Electricity*. Versailles, France, ICAE, 655–656.
- Thomas, R. J., P. R. Krehbiel, W. Rison, S. J. Hunyady, W. P. Winn, T. Hamlin, and J. Harlin, 2004: Accuracy of the Lightning Mapping Array. *J. Geophys. Res.*, **109**, D14207, doi: 10.1029/2004JD004549.
- Weisman, M. L., W. C. Skamarock, and J. B. Klemp, 1997: The resolution dependence of explicitly modeled convective systems. *Mon. Wea. Rev.*, **125**, 527–548.
- Williams, E., B. Boldi, A. Matlin, M. Weber, S. Hodanish, D. Sharp, S. Goodman, R.

Raghavan, and D. Buechler, 1999: The behavior of total lightning activity in severe Florida thunderstorms. *Atmos. Res.*, **51**, 245-265.

## TABLES

Table 1: Model numerical and physical parameters.

TABLE 1

## Model numerical and physical parameters

---

Parameter	Value
Horizontal resolution $\Delta x, \Delta y$	2000 m
Number of vertical sigma levels	51
Large time step $\Delta t$	12.0 s
Dynamical core	Eulerian mass
PBL turbulence scheme	YSU
Shortwave radiation scheme	Dudhia
Longwave radiation scheme	RRTM
Land surface model scheme	Noah
Microphysics scheme	WSM6, graupel
Graupel density	300 kg m <sup>-3</sup>
Basic initialization fields	AWIP212 NCEP EDAS
Extra initialization data used	METAR, ACARS, WSR88D
Lateral boundary conditions	Eta 3-h forecasts

---

YSU = Yonsei University Scheme

RRTM = Rapid Radiative Transfer Model

METAR = regular hourly surface aviation weather observations

ACARS = Aircraft Communications Addressing and Reporting System

## FIGURE CAPTIONS

FIG. 1. Calibration scatterplot comparing domainwide maxima for observed LMA flash rate density (y-axis; units are flashes  $(5 \text{ min})^{-1}$  per grid box column) and WRF-simulated proxy data for lightning threat method 1 (x-axis; units are  $\text{m s}^{-1}$ ), based on WRF-derived graupel flux at the  $-15^\circ\text{C}$  level. A straight line passing through the origin and having a slope of 0.042 fits the data well.

FIG. 2. Calibration scatterplot comparing domainwide maxima for observed LMA flash rate density (y-axis; units are flashes  $(5 \text{ min})^{-1}$  per grid box column) and WRF-simulated proxy data for lightning threat method 2 (x-axis, units are  $\text{kg m}^{-2}$ ), based on WRF-derived vertically integrated ice. A straight line passing through the origin and having a slope of 0.20 fits the data well.

FIG. 3. WRF skew-T log-p sounding at (latitude, longitude) = (34.4, -88.1), at 0300 UTC 30 March 2002, showing surface-based pseudoadiabatic CAPE greater than  $2000 \text{ J kg}^{-1}$  in the warm sector southwest of an observed tornadic supercell. Wind vectors are shown on the staff at right, with each full barb equal to  $5 \text{ m s}^{-1}$  of windspeed.

FIG. 4. Low-level radar reflectivity from KHTX Doppler radar at 0400 UTC 30 March 2002 (grayshades), and LMA-derived integrated flash extent density (contours) for a 5-min period at the same time. Flash extent density is depicted for clarity, although all calibrations and predictions of lightning threat are based on observations of flash origin density.

FIG. 5. WRF-derived reflectivity at the  $-15^\circ\text{C}$  level at 0400 UTC 30 March 2002 (grayshades), and WRF-predicted flash origin density (contours) for a 5-min period at the same time, based on WRF graupel flux at the  $-15^\circ\text{C}$  level. Instantaneous areal cover-



age of predicted flash density is printed at the bottom of the figure.

FIG. 6. WRF-derived anvil-level cloud ice field at 0400 UTC 30 March 2002 (grayshades), and WRF-predicted flash origin density (contours) for a 5-min period at the same time, based on WRF vertically integrated ice mixing ratios. Instantaneous areal coverage of predicted flash density is printed at the bottom of the figure.

FIG. 7. Time series plots of domainwide peak observed LMA flash origin density and predicted flash origin density based on two proxies: graupel flux (THREAT1) and vertically integrated ice content (THREAT2), for the 30 March 2002 case. Time series data symbols are explained on the figure.

FIG. 8. Time series plots of domainwide areal coverage fractions of LMA flash extent density and predicted flash origin density based on two proxies: graupel flux (THREAT1) and vertically integrated ice content (THREAT2), for the 30 March 2002 case. Time series data symbols are explained on the figure.

FIG. 9. WRF skew-T log-p sounding at (latitude, longitude) = (34.8, -85.9), at 1800 UTC 10 December 2004, showing surface-based pseudoadiabatic CAPE near  $500 \text{ J kg}^{-1}$  in the vicinity of an observed postfrontal hailstorm. Wind vectors are shown on the staff at right, with each full barb equal to  $5 \text{ m s}^{-1}$  of windspeed.

FIG. 10. Low-level radar reflectivity from KHTX Doppler radar at 1900 UTC 10 December 2004 (grayshades), and LMA-derived integrated flash extent density (contours) for a 5-min period at the same time. Flash extent density is depicted for clarity, although all calibrations and predictions of lightning threat are based on observations of flash origin density.

FIG. 11. As in Fig. 5, but for 1900 UTC 10 December 2004 case.

FIG. 12. As in Fig. 6, but for 1900 UTC 10 December 2004 case.

FIG. 13. As in Fig. 7, but for 1200-2000 UTC 10 December 2004 case.

FIG. 14. As in Fig. 8, but for 1200-2000 UTC 10 December 2004 case.

FIG. 15. As in Fig. 5, but for blended threat (THREAT3), 0400 UTC 30 March 2002 case.

FIG. 16. As in Fig. 7, but for blended threat (THREAT3), 0000-0600 UTC 30 March 2002 case.

FIG. 17. As in Fig. 8, but for blended threat (THREAT3), 0000-0600 UTC 30 March 2002 case.

FIG. 18. As in Fig. 5, but for blended threat (THREAT3), 1900 UTC 10 December 2004 case.

FIG. 19. As in Fig. 7, but for blended threat (THREAT3), 1200-2000 UTC 10 December 2004 case.

FIG. 20. As in Fig. 8, but for blended threat (THREAT3), 1200-2000 UTC 10 December 2004 case.

Threat1 Max, Graupel Flux at T = -15C

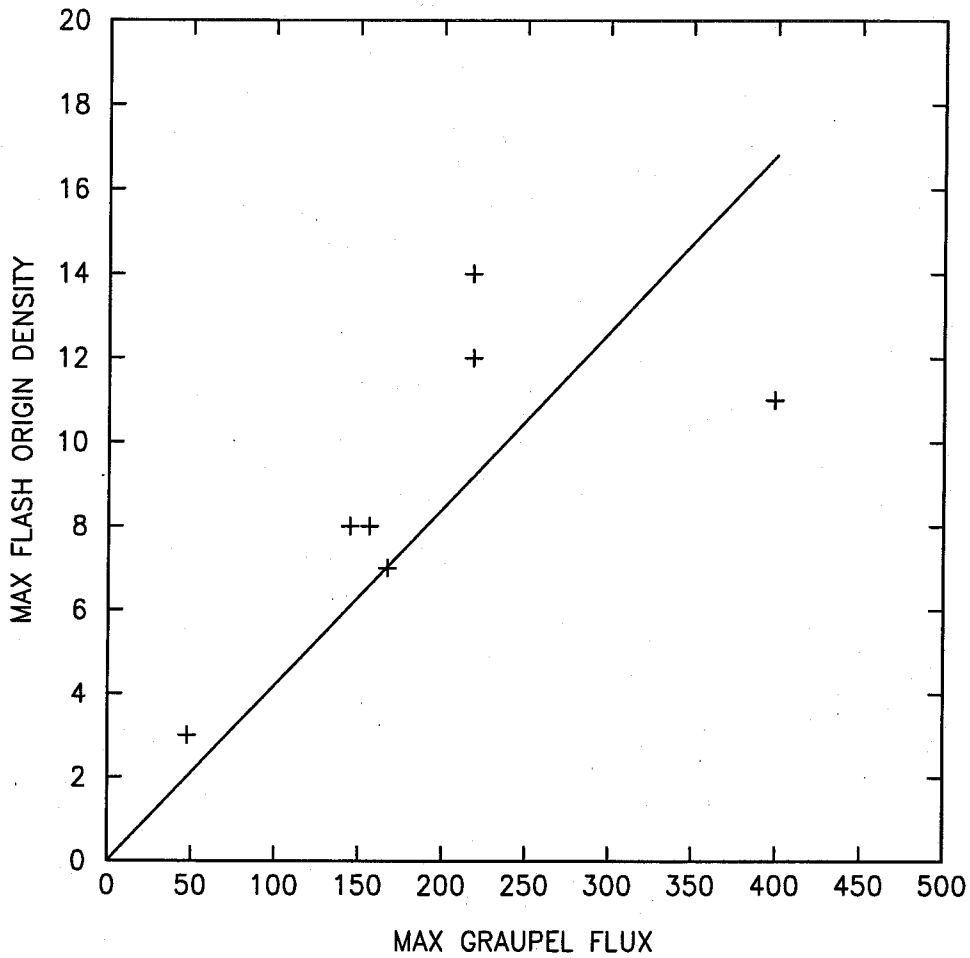


FIG. 1. Calibration scatterplot comparing domainwide maxima for observed LMA flash rate density (y-axis; units are flashes  $(5 \text{ min})^{-1}$  per grid box column) and WRF-simulated proxy data for lightning threat method 1 (x-axis; units are  $\text{m s}^{-1}$ ), based on WRF-derived graupel flux at the  $-15^{\circ}\text{C}$  level. A straight line passing through the origin and having a slope of 0.042 fits the data well.

## Threat2 Max, Vert Integrated Ice

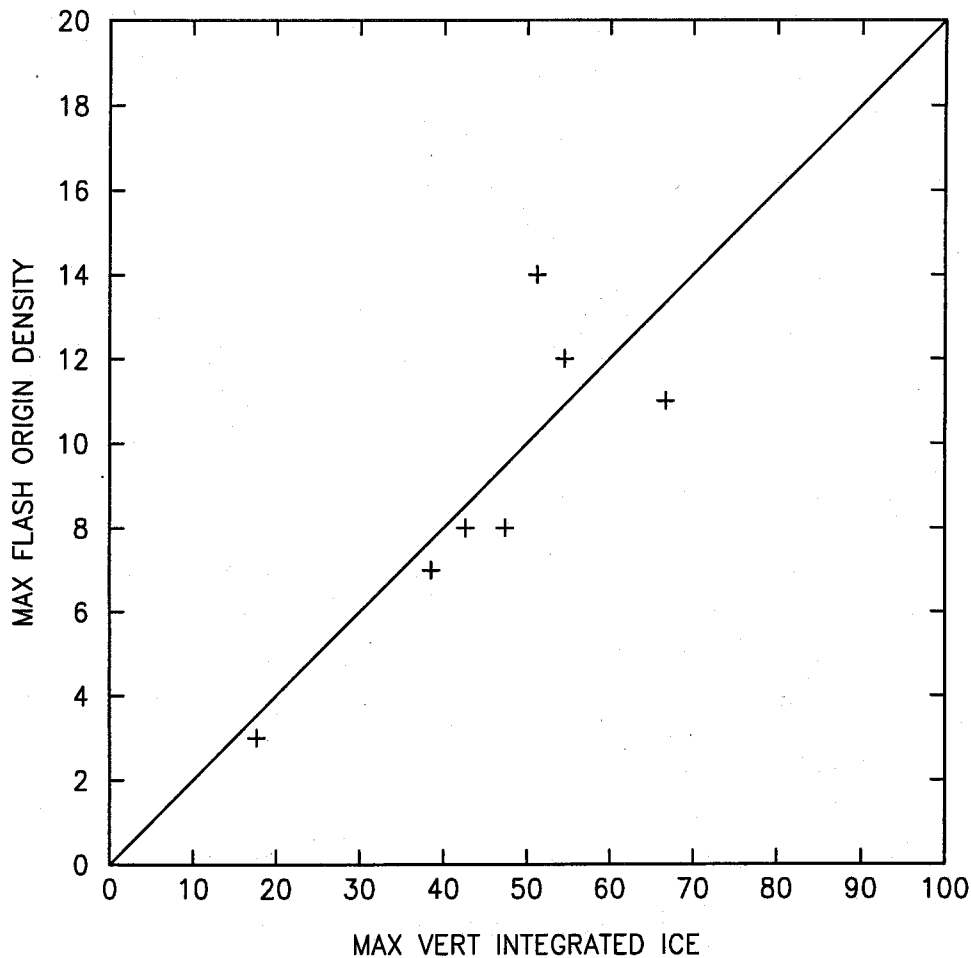


FIG. 2. Calibration scatterplot comparing domainwide maxima for observed LMA flash rate density (y-axis; units are flashes  $(5 \text{ min})^{-1}$  per grid box column) and WRF-simulated proxy data for lightning threat method 2 (x-axis, units are  $\text{kg m}^{-2}$ ), based on WRF-derived vertically integrated ice. A straight line passing through the origin and having a slope of 0.20 fits the data well.

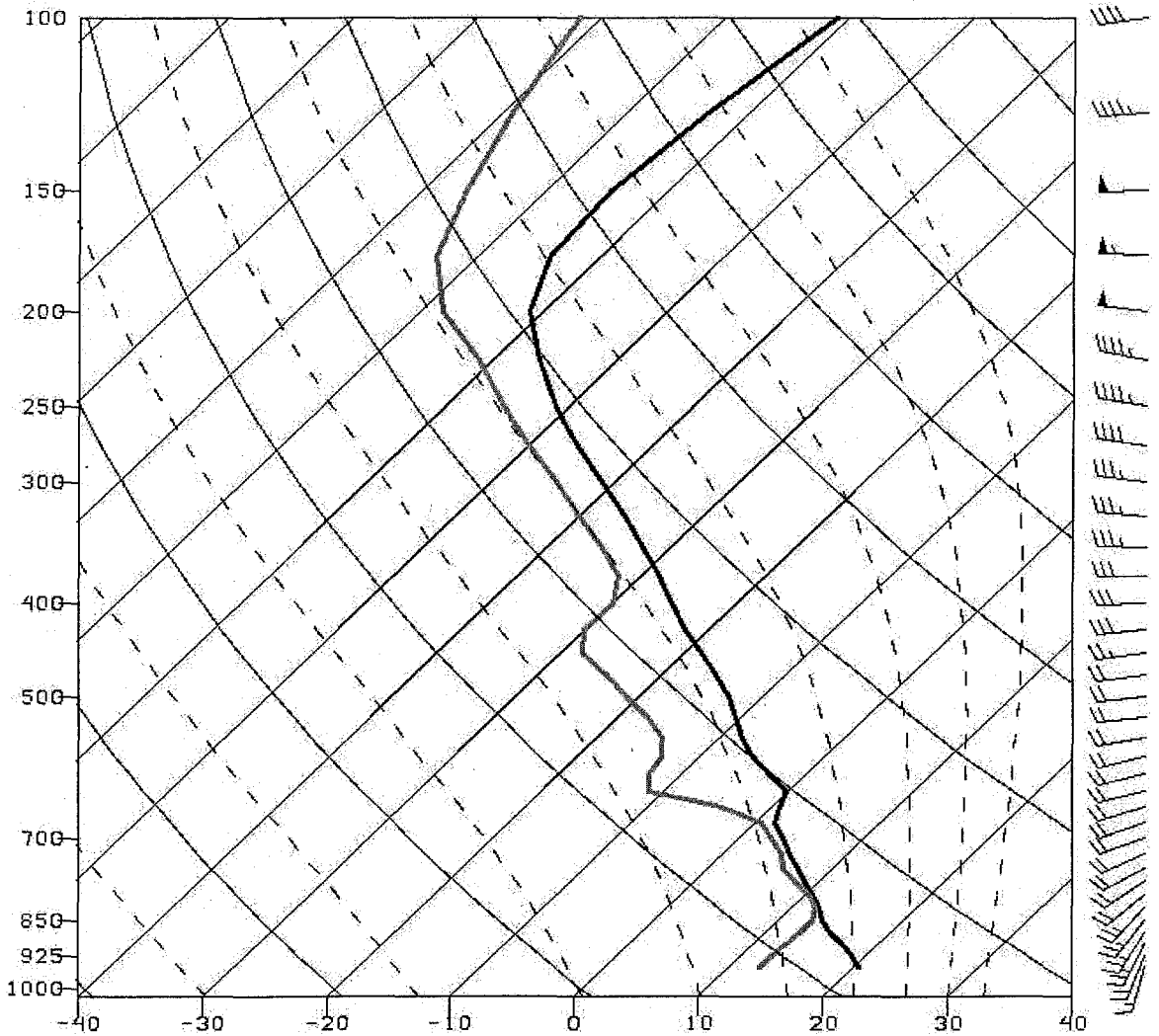


FIG. 3. WRF skew-T log-p sounding at (latitude, longitude) = (34.4, -88.1), at 0300 UTC 30 March 2002, showing surface-based pseudoadiabatic CAPE greater than  $2000 \text{ J kg}^{-1}$  in the warm sector southwest of an observed tornadic supercell. Wind vectors are shown on the staff at right, with each full barb equal to  $5 \text{ m s}^{-1}$  of windspeed.

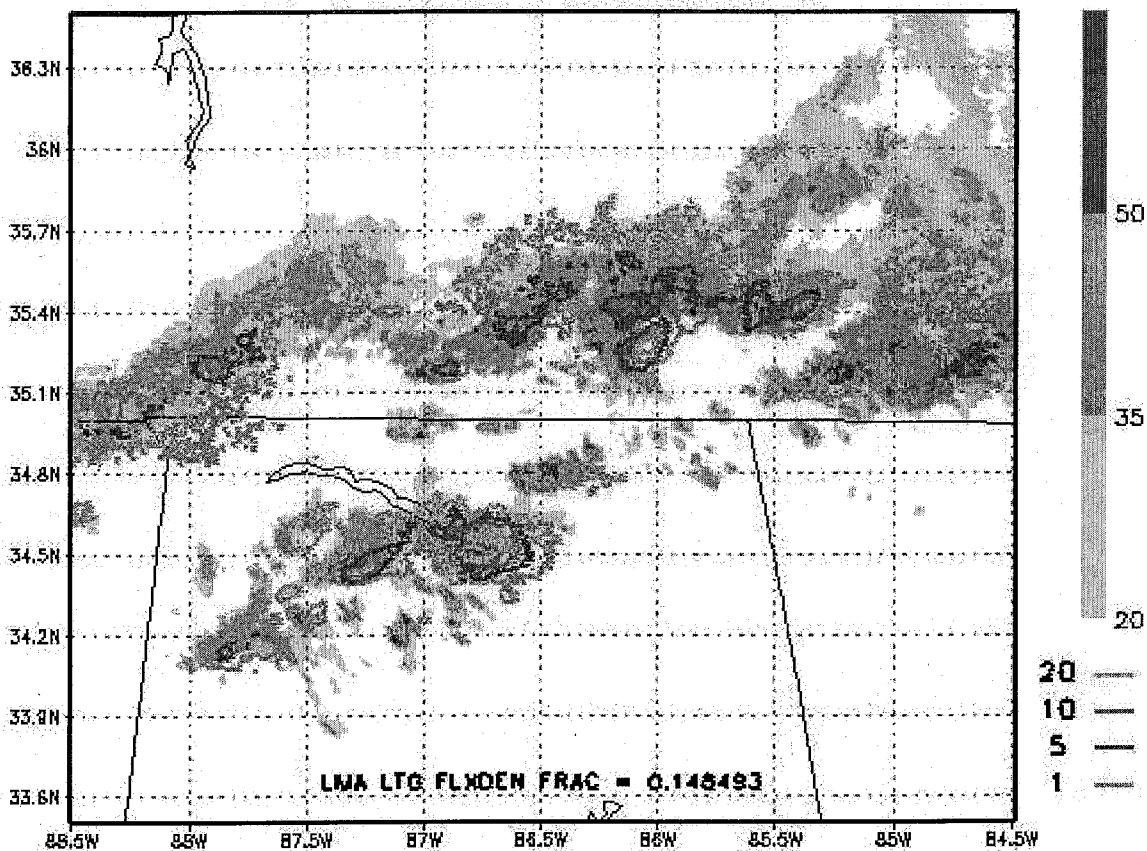


FIG. 4. Low-level radar reflectivity from KHTX Doppler radar at 0400 UTC 30 March 2002 (grayshades), and LMA-derived integrated flash extent density (contours) for a 5-min period at the same time. Flash extent density is depicted for clarity, although all calibrations and predictions of lightning threat are based on observations of flash origin density.

WRF 4B2, LTG THR1, 2002033004Z

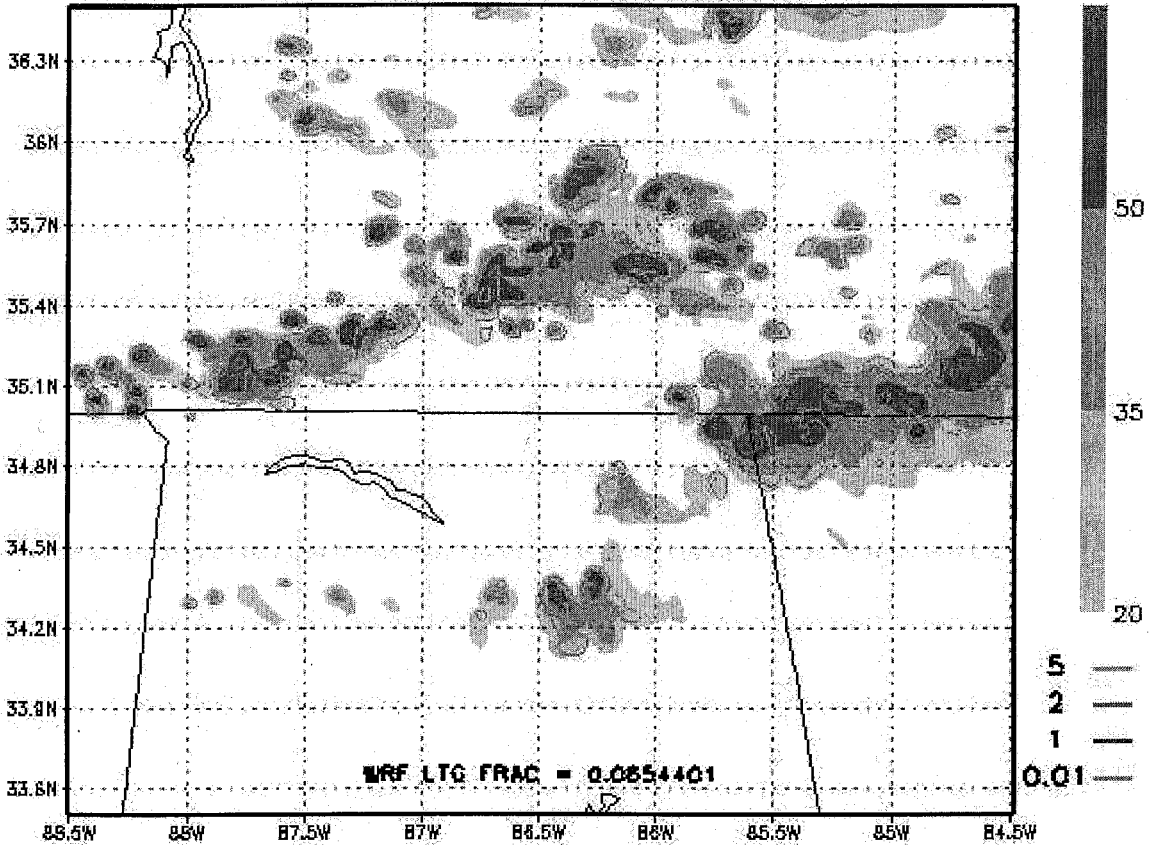


FIG. 5. WRF-derived reflectivity at the  $-15^{\circ}\text{C}$  level at 0400 UTC 30 March 2002 (grayshades), and WRF-predicted flash origin density (contours) for a 5-min period at the same time, based on WRF graupel flux at the  $-15^{\circ}\text{C}$  level. Instantaneous areal coverage of predicted flash density is printed at the bottom of the figure.

WRF ANVIL, LTG THR2, 2002033004Z

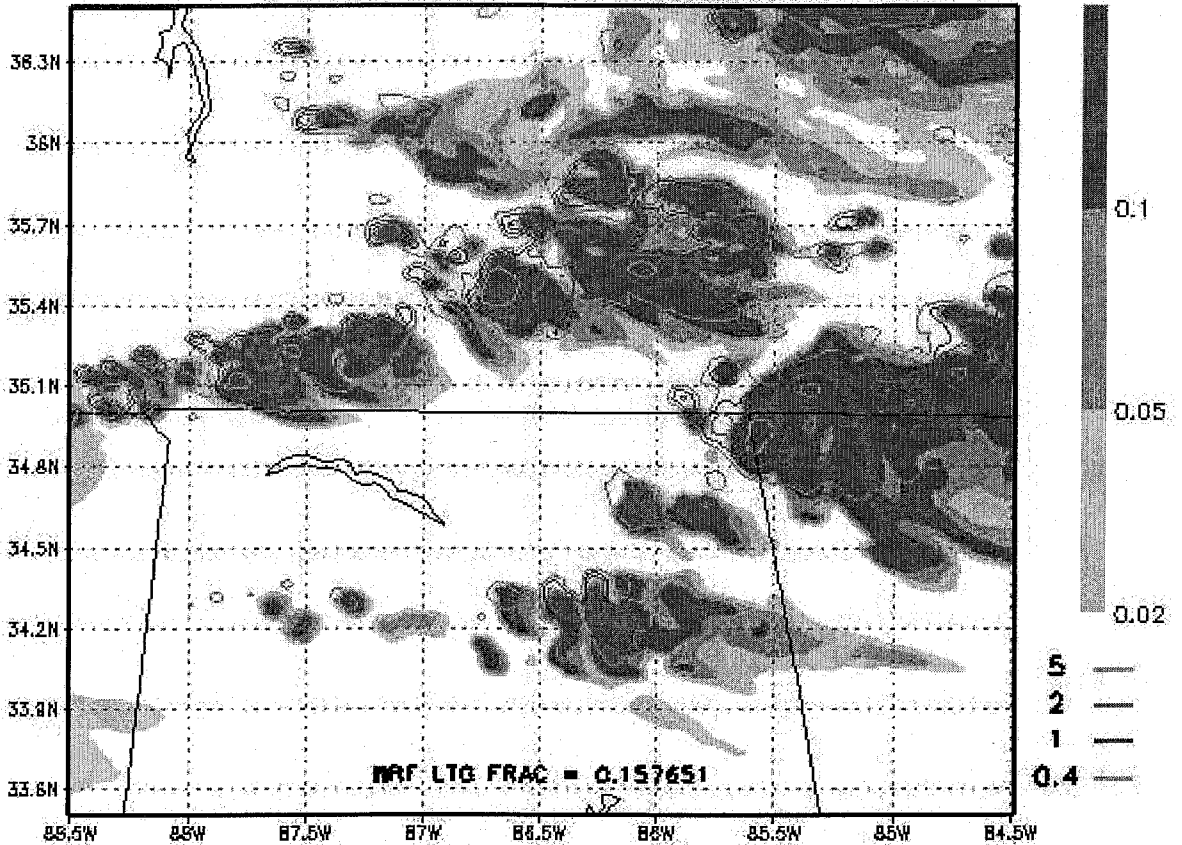


FIG. 6. WRF-derived anvil-level cloud ice mixing ratio at 0400 UTC 30 March 2002 (grayshades), and WRF-predicted flash origin density (contours) for a 5-min period at the same time, based on WRF vertically integrated ice content. Instantaneous areal coverage of predicted flash density is printed at the bottom of the figure.



# LMA, WRF PEAK FLASH DEN vs time, 20020330

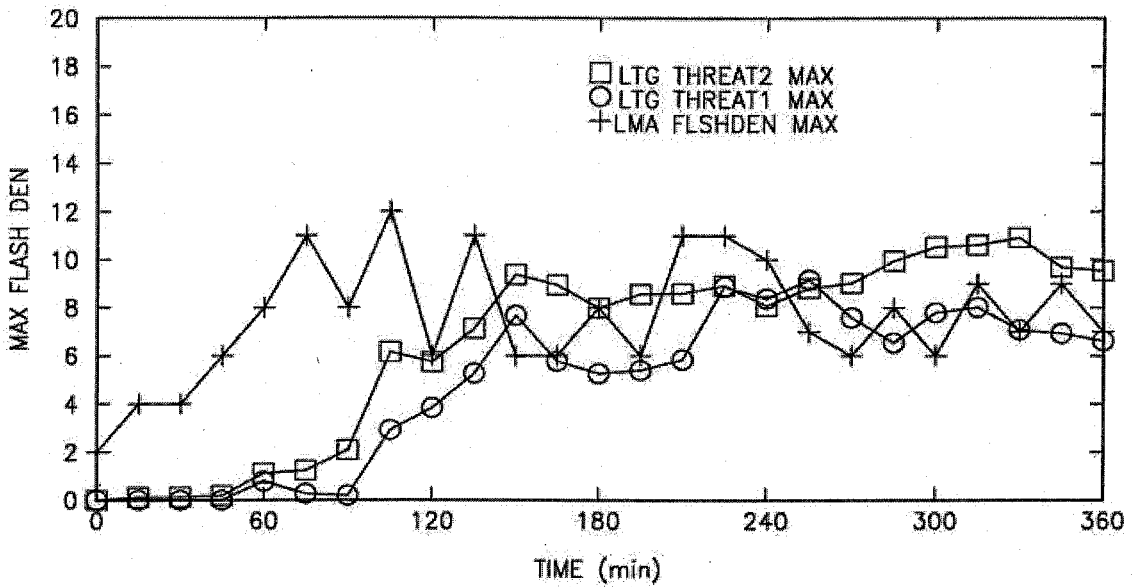


FIG. 7. Time series plots of domainwide peak observed LMA flash origin density and predicted flash origin density based on two proxies: graupel flux (THREAT1) and vertically integrated ice content (THREAT2), for the 30 March 2002 case. Time series data symbols are explained on the figure.

# LMA, WRF FLASH AREA FRAC vs time, 20020330

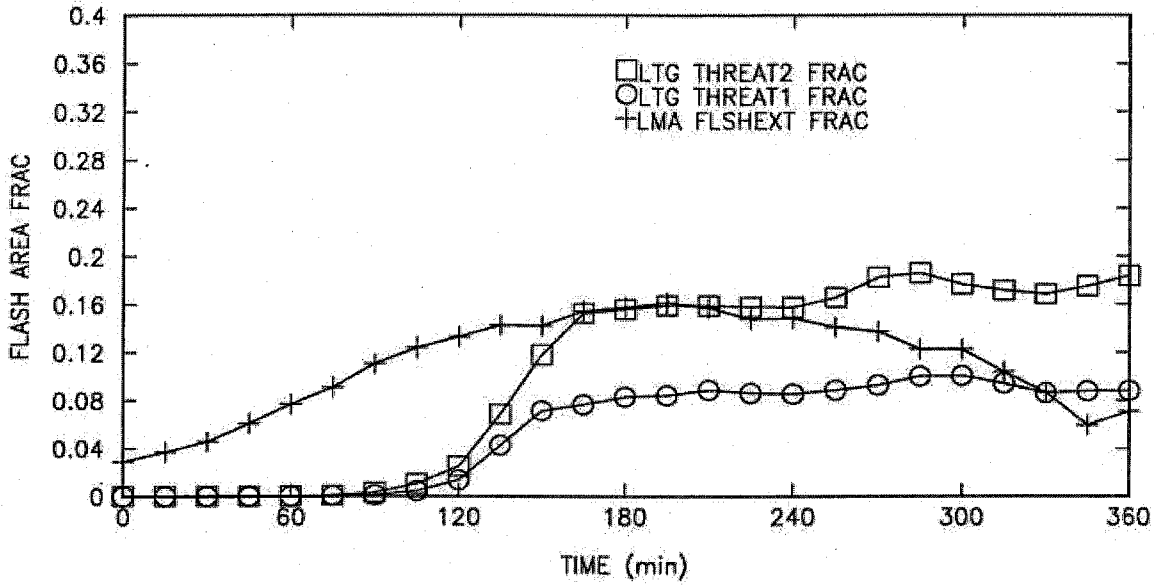


FIG. 8. Time series plots of domainwide areal coverage fractions of LMA flash extent density and predicted flash origin density based on two proxies: graupel flux (THREAT1) and vertically integrated ice content (THREAT2), for the 30 March 2002 case. Time series data symbols are explained on the figure.

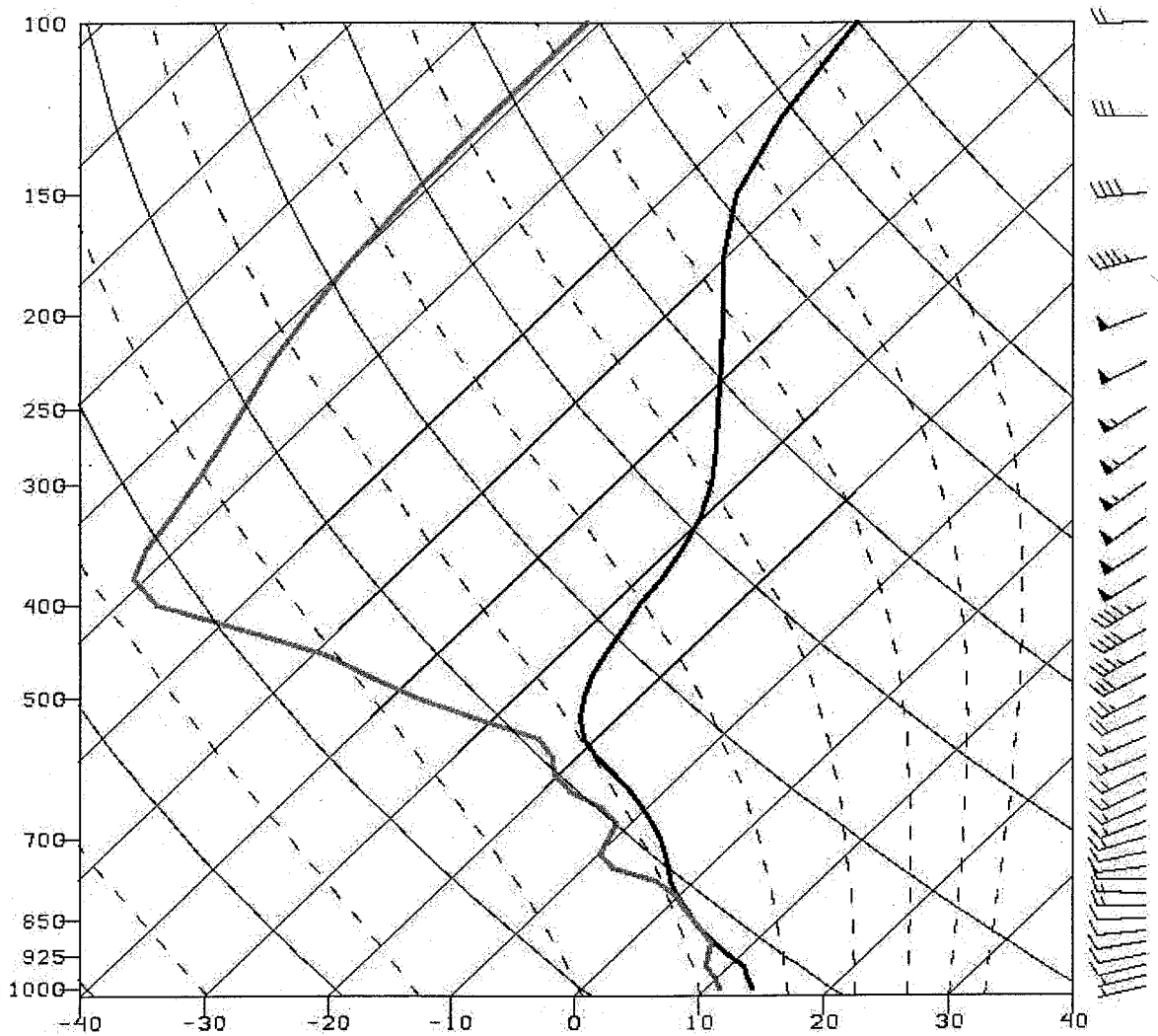


FIG. 9. WRF skew-T log-p sounding at (latitude, longitude) = (34.8, -85.9), at 1800 UTC 10 December 2004, featuring surface-based pseudoadiabatic CAPE near  $500 \text{ J kg}^{-1}$  in the vicinity of an observed postfrontal hailstorm. Wind vectors are shown on the staff at right, with each full barb equal to  $5 \text{ m s}^{-1}$  of windspeed.

KHTX dBZ, LMA LTG. 2004121019Z

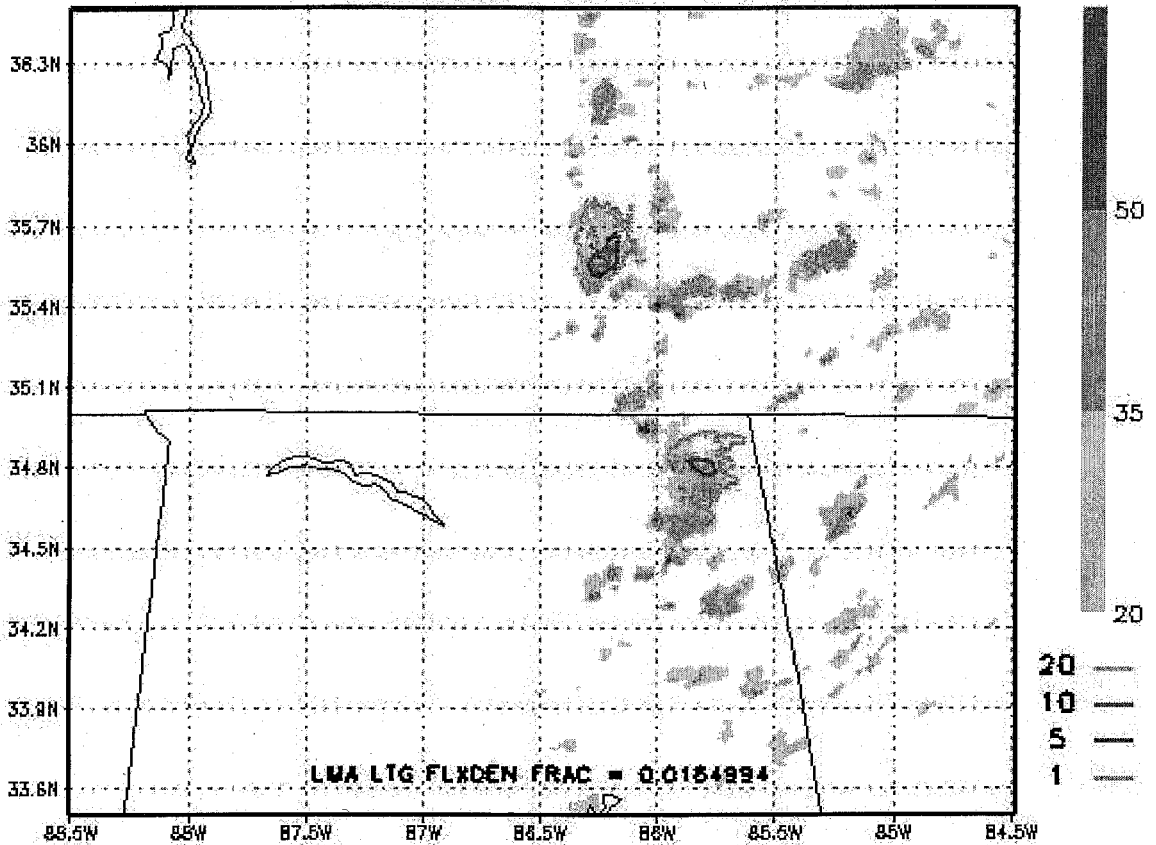


FIG. 10. Low-level radar reflectivity from KHTX Doppler radar at 1900 UTC 10 December 2004 (grayshades), and LMA-derived integrated flash extent density (contours) for a 5-min period at the same time. Flash extent density is depicted for clarity, although all calibrations and predictions of lightning threat are based on observations of flash origin density.

WRF dBZ, LTG THR1, 2004121019Z

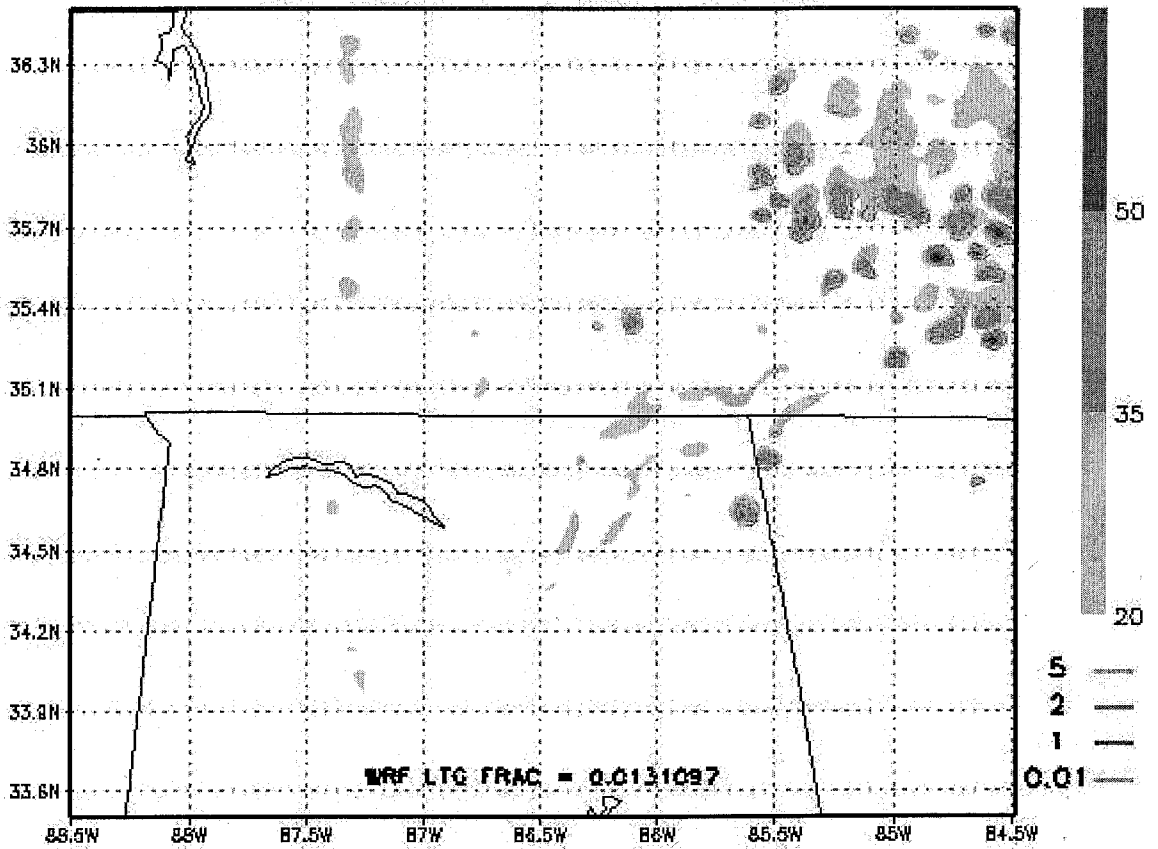


FIG. 11. WRF-derived reflectivity at the  $-15^{\circ}\text{C}$  level at 1900 UTC 10 December 2004 (grayshades), and WRF-predicted flash origin density (contours) for a 5-min period at the same time, based on WRF graupel flux at the  $-15^{\circ}\text{C}$  level. Instantaneous areal coverage of predicted flash density is printed at the bottom of the figure.

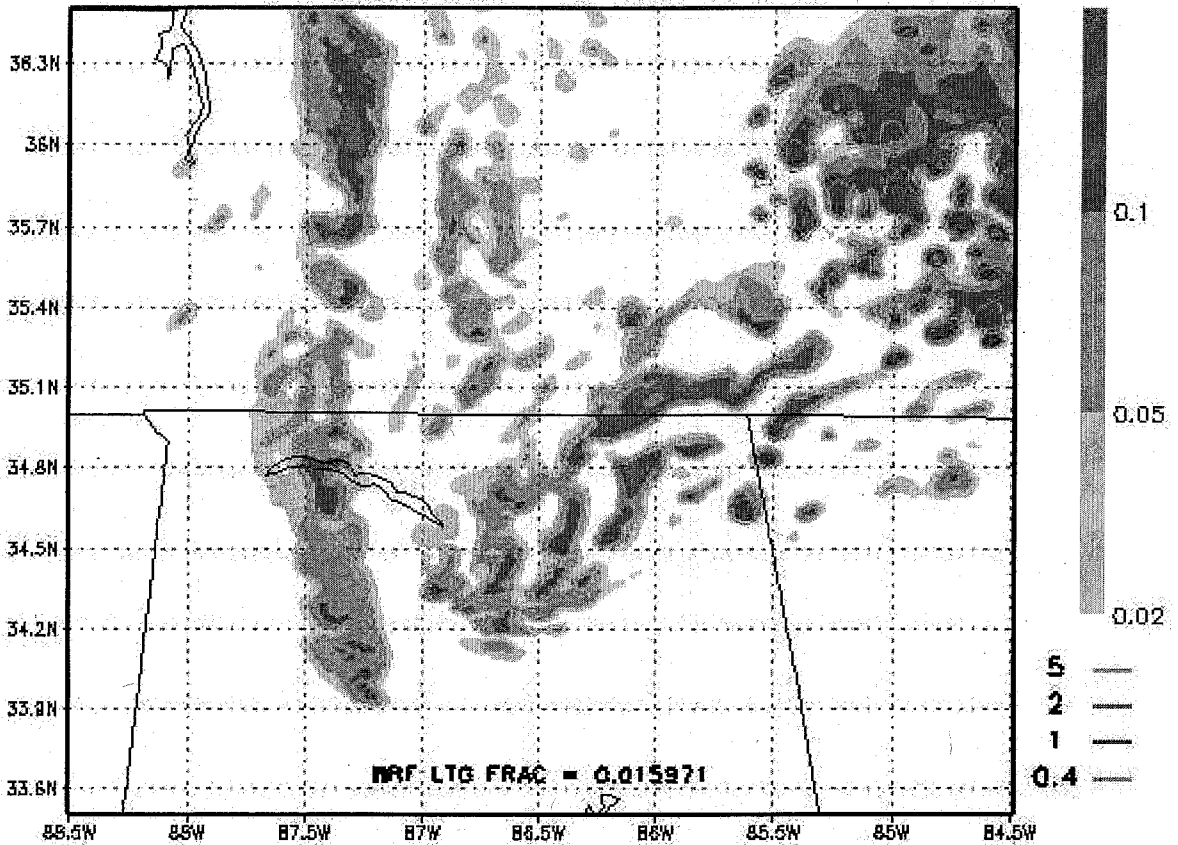


FIG. 12. WRF-derived anvil-level cloud ice mixing ratio at 1900 UTC 10 December 2004 (grayshades), and WRF-predicted flash origin density (contours) for a 5-min period at the same time, based on WRF vertically integrated ice content. Instantaneous areal coverage of predicted flash density is printed at the bottom of the figure.

# LMA, WRF PEAK FLASH DEN vs time, 20041210

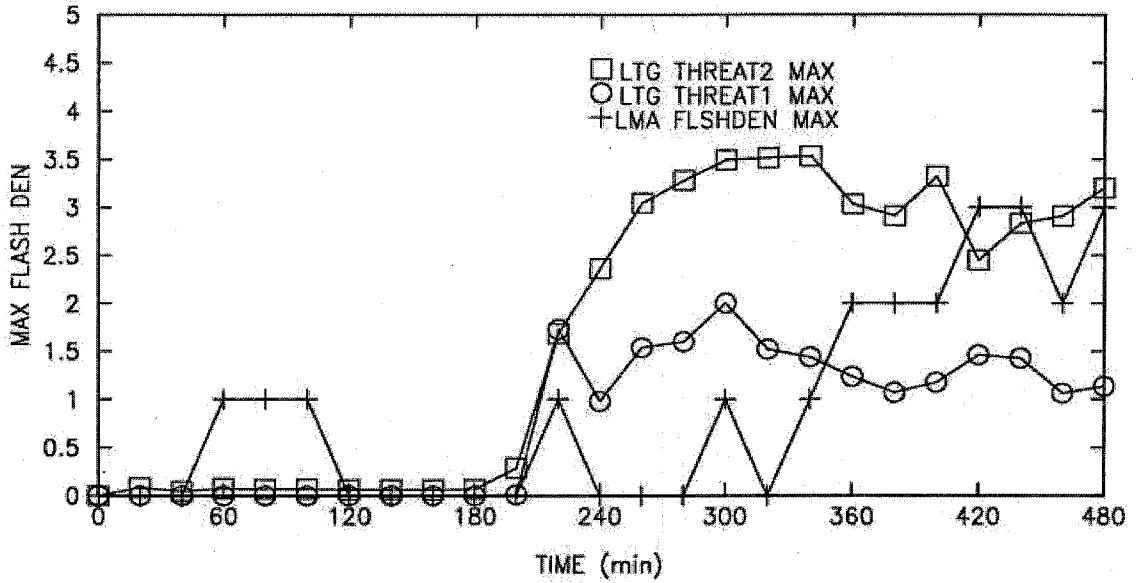


FIG. 13. Time series plots of domainwide peak observed LMA flash origin density and predicted flash origin density based on two proxies: graupel flux (THREAT1) and vertically integrated ice content (THREAT2), for the 10 December 2004 case. Time series data symbols are explained on the figure.

# LMA, WRF FLASH AREA FRAC vs time, 20041210

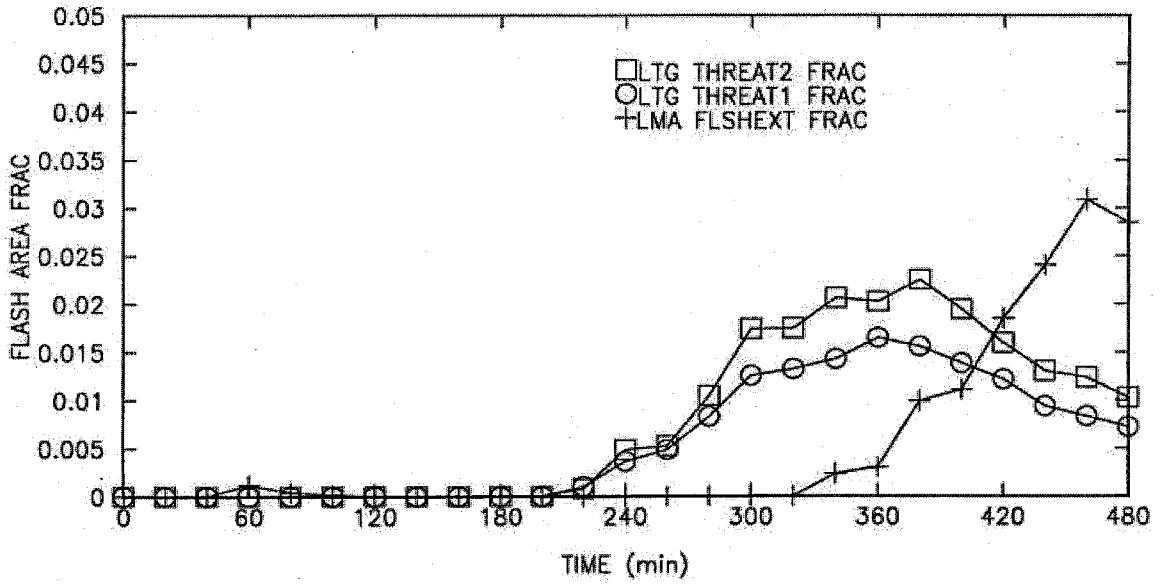


FIG. 14. Time series plots of domainwide areal coverage fractions of LMA flash extent density and predicted flash origin density based on two proxies: graupel flux (THREAT1) and vertically integrated ice content (THREAT2), for the 10 December 2004 case. Time series data symbols are explained on the figure.



WRF 4BZ, LTG THREAT3, 2002033004Z

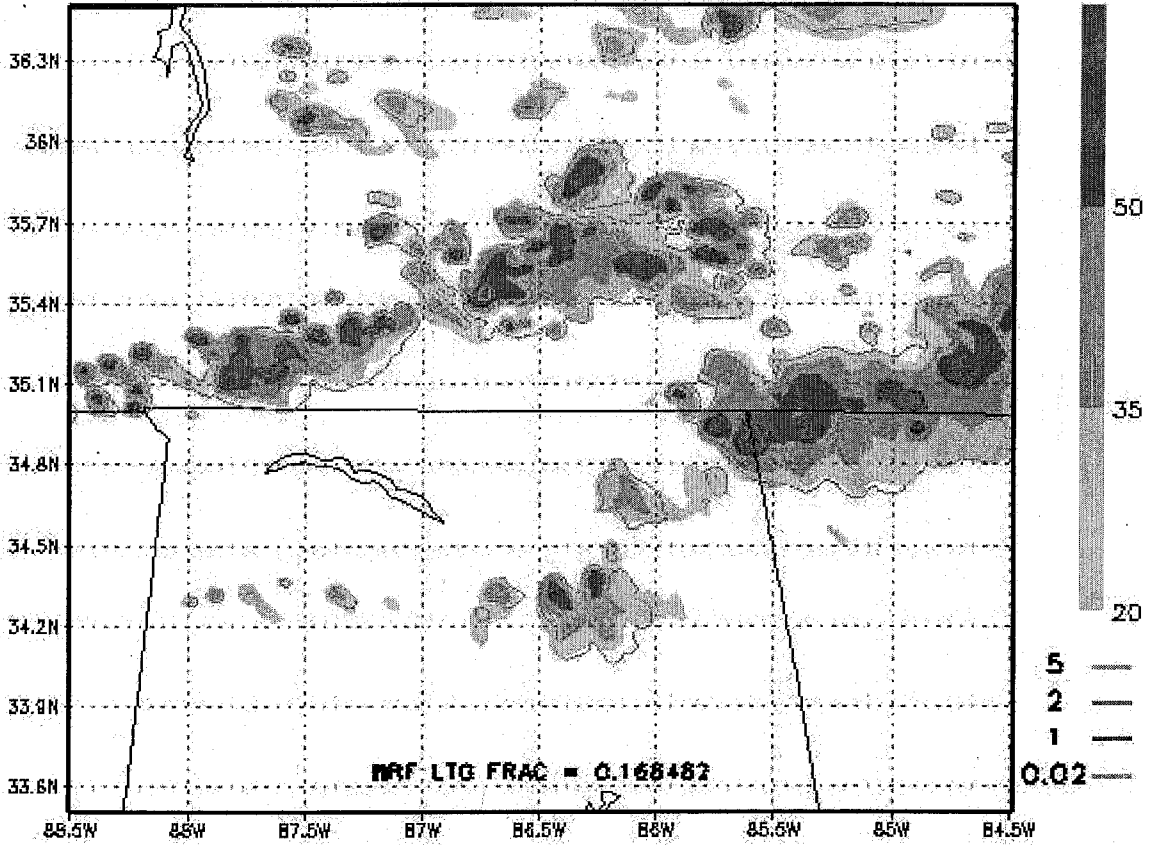


FIG. 15. As in Fig. 5, but for blended threat (THREAT3), 0400 UTC 30 March 2002 case.

LMA, WRF PEAK FLASH DEN vs time, 20020330

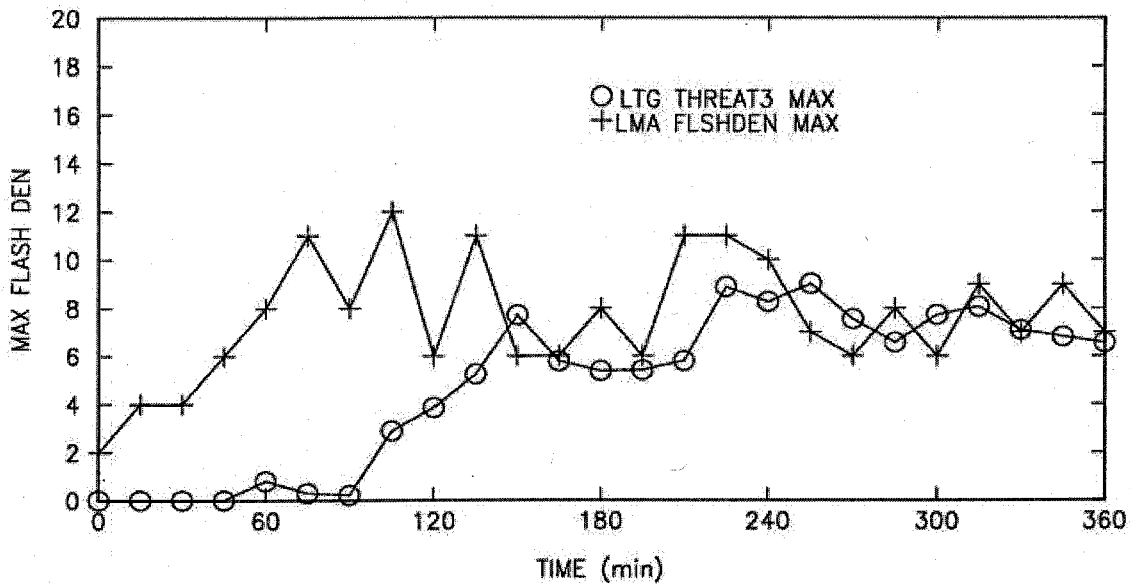


FIG. 16. As in Fig. 7, but for blended threat (THREAT3), 0000-0600 UTC 30 March 2002 case.

# LMA, WRF FLASH AREA FRAC vs time, 20020330

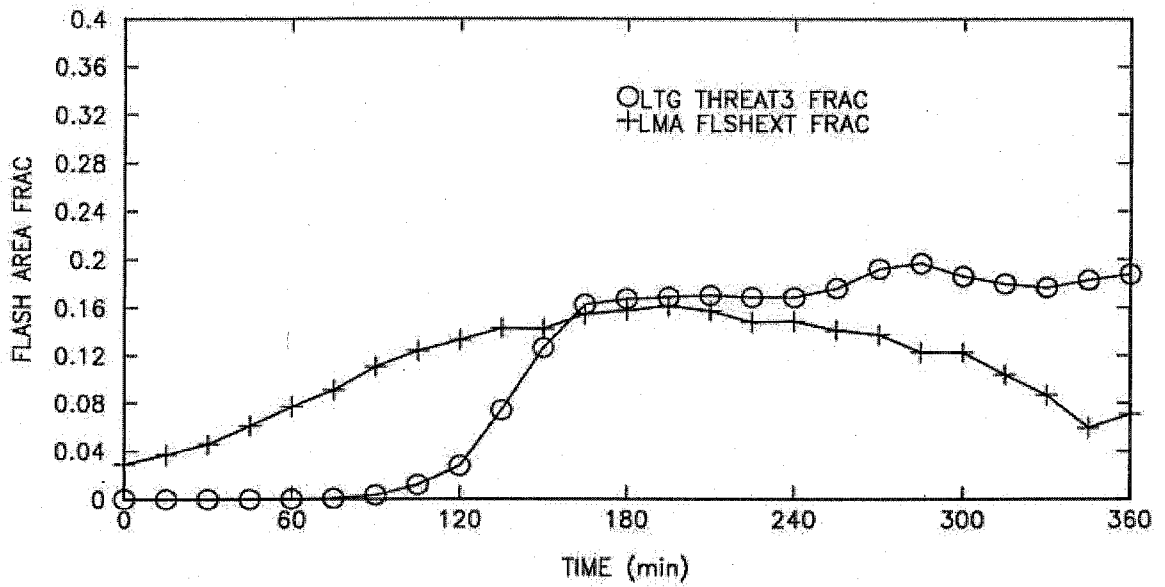


FIG. 17. As in Fig. 8, but for blended threat (THREAT3), 0000-0600 UTC 30 March 2002 case.

WRF 4BZ, LTG THREAT3, 2004121019Z

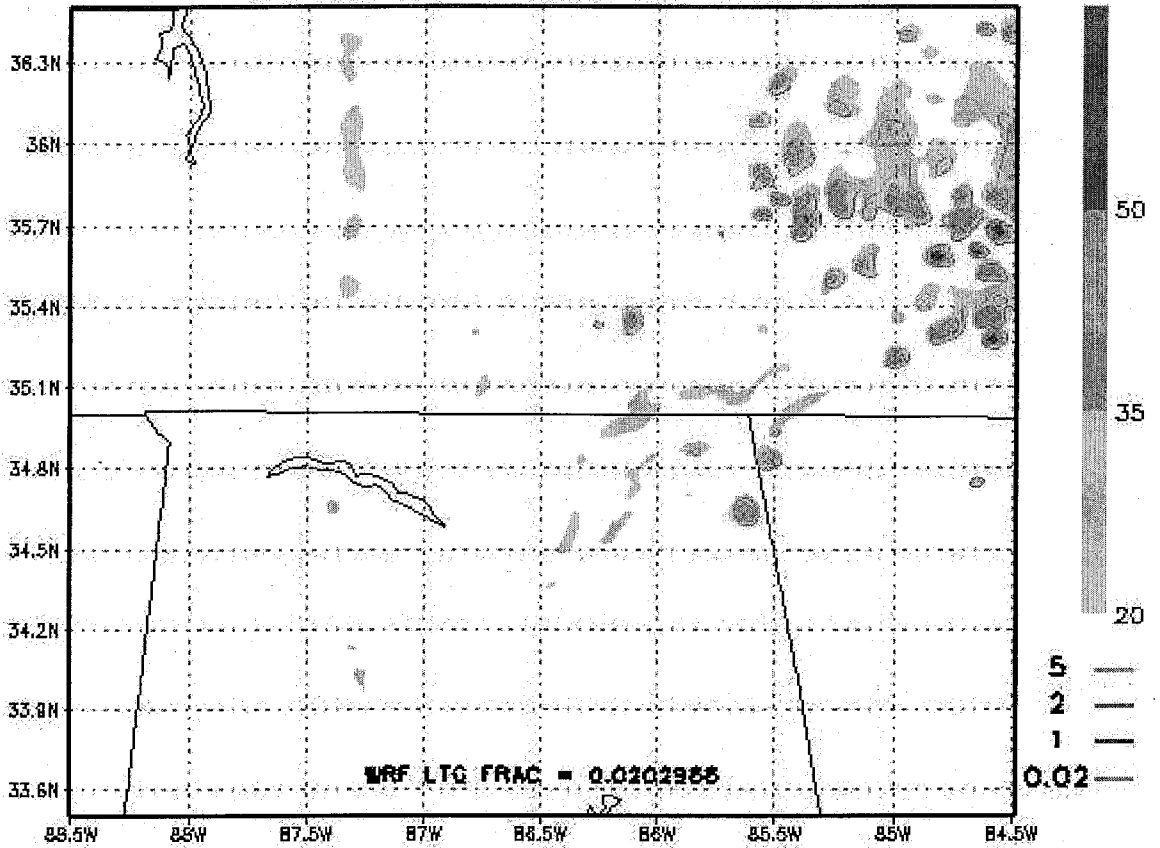


FIG. 18. As in Fig. 5, but for blended threat (THREAT3), 1900 UTC 10 December 2004 case.

# LMA, WRF PEAK FLASH DEN vs time, 20041210

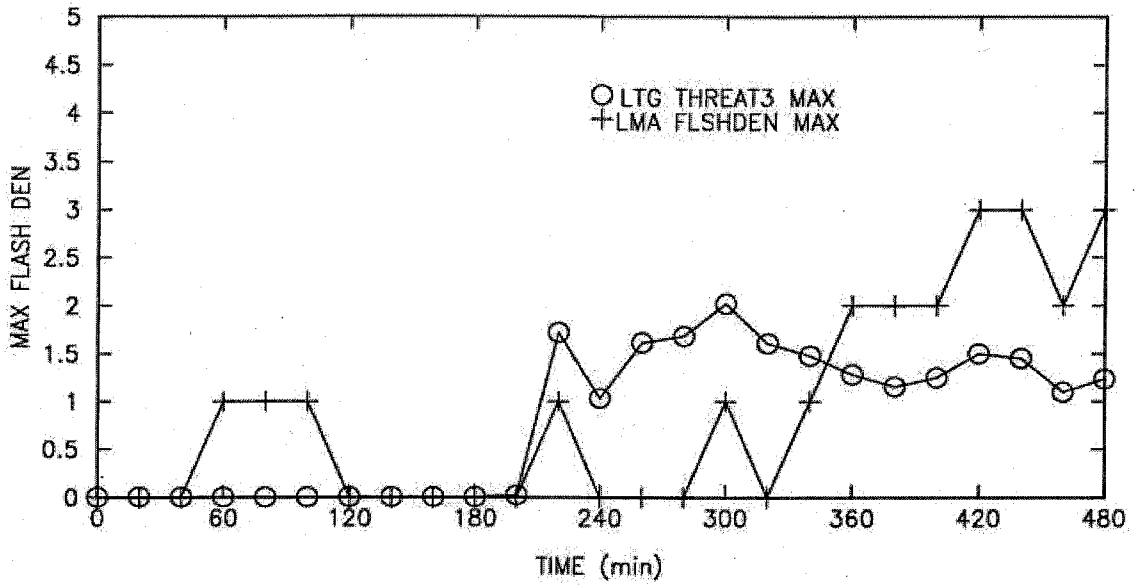


FIG. 19. As in Fig. 7, but for blended threat (THREAT3), 1200-2000 UTC 10 December 2004 case.

LMA, WRF FLASH AREA FRAC vs time, 20041210

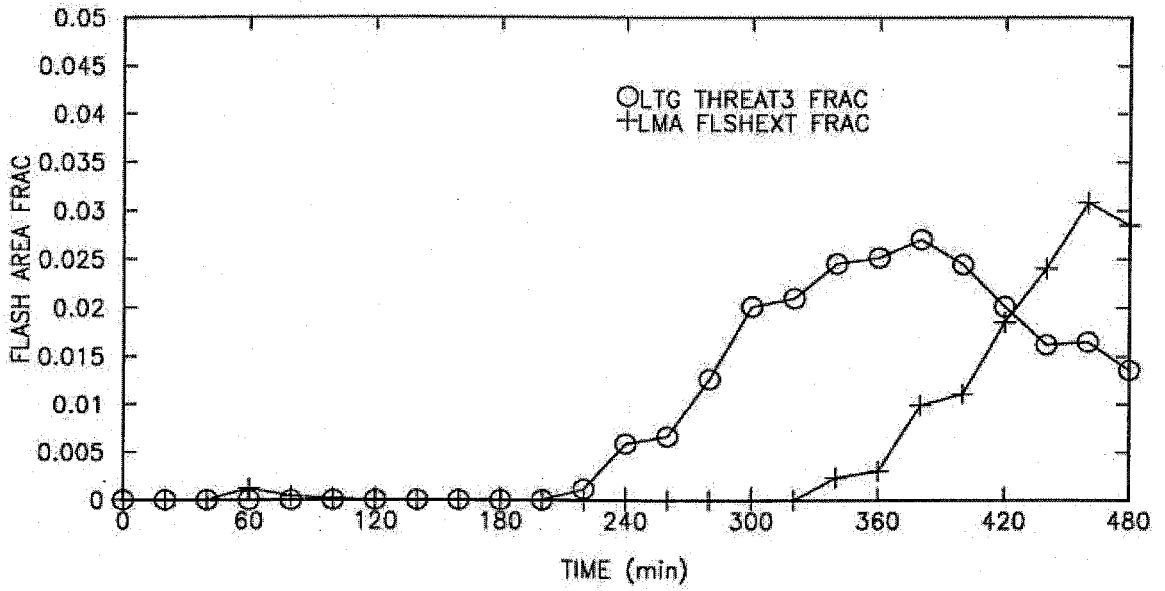


FIG. 20. As in Fig. 8, but for blended threat (THREAT3), 1200-2000 UTC 10 December 2004 case.